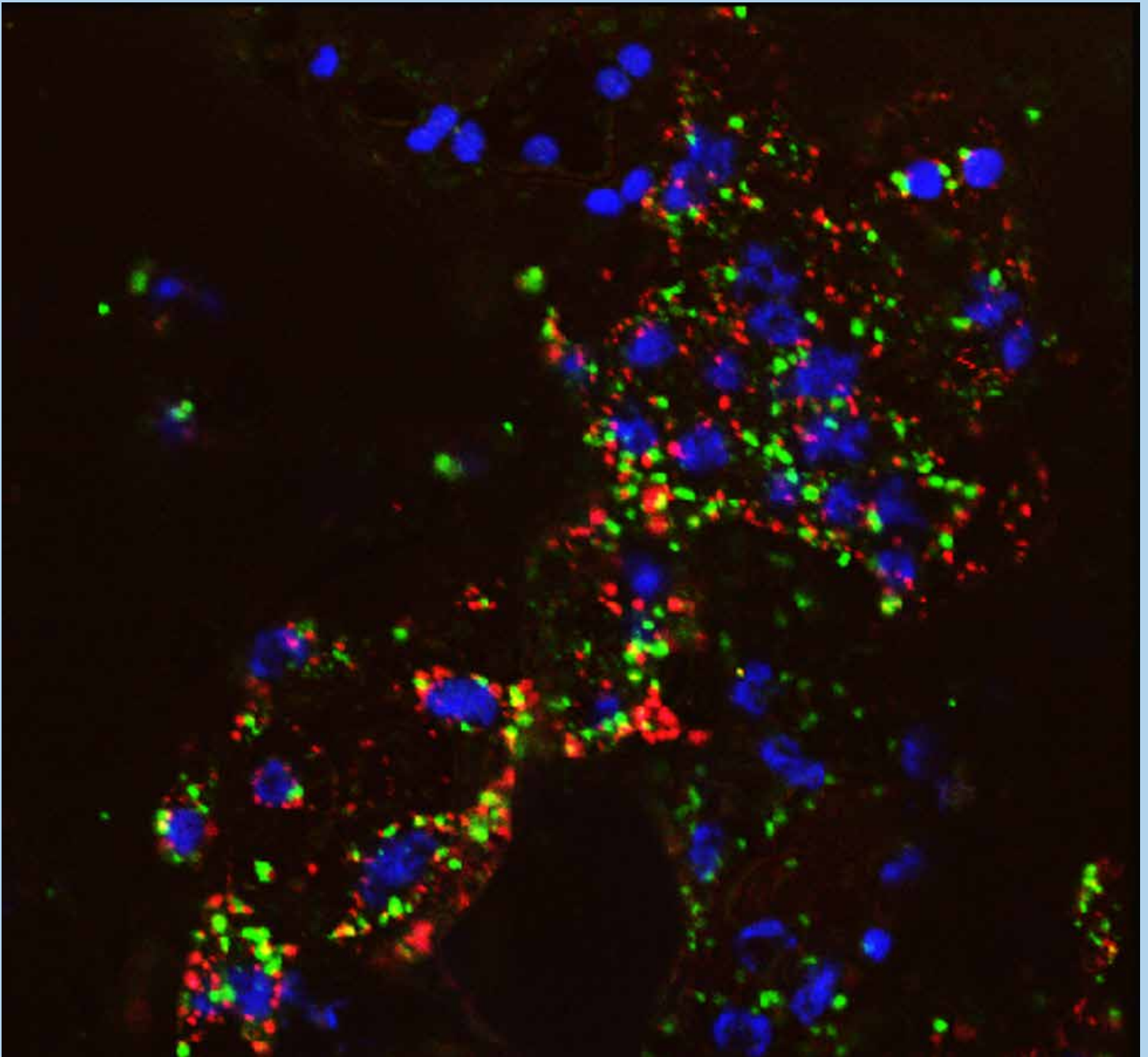


Texas Journal of Microscopy



Volume 52,
Number 1, 2021
ISSN 1554-0820

Visit our website at www.texasmicroscopy.org



Fungus Gnats - Dr. Peter H. Kerr
Plant Pest Diagnostics Branch, California Department of Food & Agriculture

Fractal Nanotrous
Caltech, Materials Science and Mechanics (Julia R. Greer & Co-workers)

Multi-Application Autosamdri®-931 CPD System

- ✓ *NEW ! Post Process Data Review Feature*
- ✓ *Default "Automode" Setting Suitable for Most Applications*
- ✓ *Patent Pending "Stasis Software" for Challenging Sample Types*
- ✓ *Automatic & Custom Programmable Recipe Capability*
- ✓ *Available in Three Chamber Sizes*
- ✓ *Cleanroom System Options*
- ✓ *Made in U.S.A.*

TSM OFFICERS 2020-2021

President:

BERND ZECHMANN
Center for Microscopy and Imaging
Baylor University | Waco, TX 76798-7046
Phone (254) 710-2322
Email: Bernd_Zechmann@baylor.edu

President-elect:

AMY JO HAMMETT
Department of Biology
Texas Woman's University | Denton, TX, 76204-5799
Phone (940)-898-2397
Email: Ahammett1@twu.edu

Past President:

LAURA HANSON
Department of Biology
Texas Woman's University • Denton, TX 76204-5799
(940) 898-2472 • LHanson@twu.edu

Secretary:

BERND ZECHMANN
Center for Microscopy and Imaging
Baylor University | Waco, TX 76798-7046
Phone (254) 710-2322
Email: Bernd_Zechmann@baylor.edu

Secretary-elect:

VACANT

Treasurer:

DAVID GARRETT
Department of Materials Science and Engineering
University of North Texas | Denton, Texas 76203-5017
Phone (940) 369-8836
Email: Dgarrett@unt.edu

Treasurer-elect:

VACANT

Program Chairman:

NABARUN GHOSH
Dept. of Life, Earth, and Environmental Sciences
West Texas A&M University | Canyon, Texas 79015
Phone (806) 651-2571
Email: Nghosh@wtamu.edu

Program Chairperson-elect:

VACANT

APPOINTED OFFICERS

Corporate Member Representative:

JAMES C. LONG
Ted Pella, Inc.
P.O. Box 492477 | Redding, CA 96049
Phone (530) 227-8329
Email: James_Long@tedpella.com

Facebook Master:

NABARUN GHOSH
Dept. of Life, Earth, and Environmental Sciences
West Texas A&M University | Canyon, Texas 79015
Phone (806) 651-2571 FAX (806) 651-2928
Email: nghosh@wtamu.edu

Student Representative:

AUBREY HOWARD
West Texas A&M University | Canyon, Texas 79015
Phone (806) 632-9759
Email: adhoward3@buffs.wtamu.edu

Journal Editors:

CATALINA PISLARIU
Department of Biology
Texas Woman's University | Denton, TX 76204-5799
Phone (940) 898-4611
Email: cpislariu@twu.edu

Webmaster:

BERND ZECHMANN
Center for Microscopy and Imaging
Baylor University | Waco, TX 76798-7046
Phone (254) 710-2322
Email: Bernd_Zechmann@baylor.edu

Contents

TEXAS JOURNAL OF MICROSCOPY
VOLUME 52, NUMBER 1, 2021
ISSN 1554-0820



Editor

Catalina Pislariu, PhD
Department of Biology, Texas Woman's University, Denton, TX 76204

Official Journal of the Texas Society for Microscopy
"TSM - Embracing all forms of Microscopy"

www.texasmicroscopy.org

President's Message 5

In Memoriam Dr Ernest Couch 6

Spring 2021 Life Sciences Articles

EXPRESSION OF SEROTONIN RECEPTOR SUBTYPE 3A (5HT3A) ON RAT TRIGEMINAL SENSORY NEURONS
Sukhbir Kaur, Angela Lopez-Ramirez, Taylor M. Hickman, Michael P. Hunter, Dayna L. Averitt..... 8

COLORADO TICK FEVER VIRUS-INDUCED ULTRASTRUCTURAL CHANGES IN HUMAN AND MONKEY CELL LINES
Sarah Owen, Caitlyn Gaffney, Judy A. King, Rajesh P. Balarman, and Jeremy Bechelli 14

A RAPID METHOD TO CHARACTERIZE CELLULOSE FIBRILS USING SCANNING ELECTRON MICROSCOPY
Marina R. Mulenios, Bernd Zechmann, and Christie M. Sayes..... 20

MORPHOLOGICAL STUDY OF THE OVIPOSITOR OF THREE SPECIES OF *PLEIDAE* (INSECTA: HEMIPTERA) USING THE SCANNING ELECTRON MICROSCOPE
Jerry L. Cook and Rajesh Balarman..... 23

BEAM DECELERATION ENHANCES IMAGE QUALITY OF BIOLOGICAL SAMPLES IN THE SCANNING ELECTRON MICROSCOPE
William J. Matthaeus and Bernd Zechmann 28

Spring 2021 Material Science Article

IN-SITU MAGNETIZATION MAPPING OF THE MAGNETIC EVOLUTION IN NI NANOWIRES BY ELECTRON HOLOGRAPHY
Arturo Galindo, Andrei Hernandez-Robles, Eduardo Ortega, Jason Giuliani, and Arturo Ponce..... 32

Corporate Members 40

Advertiser's Index:

Tousimis 2
AMT..... 4
IXRF Systems..... 42
Nikon Instruments..... 43
RMC Boeckler 44

ON THE COVER

Subcellular localization of the MtNPD1 protein of *Medicago truncatula* (barrel medic) by confocal laser scanning microscopy. The MtNPD1 red fluorescent protein (RFP) fusion driven by the 35S Promoter was co-transformed with a Golgi apparatus marker green fluorescent protein (GFP) fusion, also driven by the 35S Promoter (35Sp::ST::sGFP) into *Nicotiana tabacum* (tobacco) leaves, by *Agrobacterium tumefaciens* transformation. Peeled epidermal cells were imaged using a Leica TCS SP2 AOBs laser-scanning confocal microscope. 35Sp::MtNPD1::RFP targets to punctate structures that do not co-localize with the Golgi apparatus marker. Shown in blue are chloroplasts. The photomicrograph was taken by Catalina Pislariu.



AMT: NanoSprint43

Unrivaled 43 Mpix Imaging for the TEM



Advanced Microscopy Techniques

242 West Cummings Park, Woburn, MA 01801

Tel: (978)774-5550 Fax: (978)739-4313

www.amtimaging.com

President's Message

As we near the end of another tumultuous year, we hope that this message finds all members of the TSM and their loved ones in good health. While 2020 and 2021 were challenging years for the executive board of the Texas Society for Microscopy, we managed to maneuver through the interruptions of the pandemic quite well. The decision of the executive board to cancel the annual meeting in 2021 kept the TSM free of any major financial commitments. In March 2020 we launched our new webpage (<https://texas.microscopy.org/>) and in May 2020 we opened the TSM Twitter account (<https://twitter.com/MicroscopyTexas>). Both platforms helped us to better connect and reach our members in times of lockdowns, travel restrictions, and social distancing.

The highlight of 2020 was, without a doubt, the 55th annual TSM meeting in March 2020, in College Station which was very well attended. In 2020, we provided 24 students with travel support, and we supported the research of Henry Lujan (Baylor University) with our Small Grant Program. In order to connect members of our society who have long been apart, the executive committee spearheaded by our secretary Bernd Zechmann held a very successful Summer Seminar Series. We hosted nine well-attended Zoom presentations throughout July 2021 on various current topics. Our society is in good financial health, the membership is strong, and we can look to a bright future.

In 2021, we unfortunately lost our beloved honorary member Dr. Ernest Couch. He was an extremely active member of the TSM and a dear friend. He served on the TSM-executive board in many different roles and influenced the TSM in many ways. He will be missed.

We would like to thank all officers for their hard work over the past two years. Thanks to our treasurer, David Garrett, the financial situation of our society is in a good state. We are grateful for the support of our past secretaries

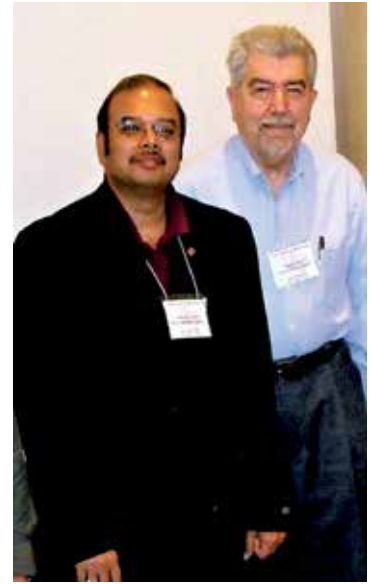
Shazia Ahmed and secretary-elect Rajesh Balaraman for managing the business and communications of the TSM, as well as Nabarun Ghosh and Rajesh Balaraman for taking care of social media for the TSM. We are also thankful for the support of James Long and Aubrey Howard, who do an amazing job representing the corporate sponsors and student members of the TSM. Lastly, we want to thank our editor, Catalina Pislariu, for organizing the review process, planning, designing, and publishing of the Texas Journal of Microscopy. Amy Jo would also like to extend much thanks to Bernd Zechmann for all of his contributions to our society and who is already planning the next annual TSM meeting at Baylor University in Waco. Finally, thank you to all of the student, regular, honorary, and corporate members for supporting the TSM.

We look forward to seeing you all in Waco next year for what will be a most joyous reunion of our members and a celebration of microscopy for the 56th annual TSM meeting!

*Amy Jo M. Hammett, TSM President 2021-2022 and
Bernd Zechmann, TSM President 2020-2021*



IN MEMORIAM DR. ERNEST COUCH



“Dr. Ernest Couch has served the Texas Society for Microscopy (TSM: <https://texas.microscopy.org/>) in several roles for many years. He was Treasurer (1973-1975), Program Chairman (1983-1985; 2011-2012), and President (2007-2008). As President, he was committed to improve long-range planning for TSM meetings, and to secure that the TSM remained a vital platform for students and young investigators. He also worked hard to recruit members from all forms of microscopy to make sure that our society becomes more inclusive. In his roles as Program Chairman and President, he organized and oversaw the organization of several important meetings (e.g. Tyler in 1983 and Fort Worth in 2012). Dr. Couch and his students have also provided countless contributions in the form of abstracts and presentations at various TSM meetings in the past. The Executive Board of the TSM awarded him honorary membership of the TSM in 2018. We offer our heartfelt sympathy to his family members for their great loss.”

TSM Executive Board

“I went to visit Dr. Neal D. Nossaman, O.D., Therapeutic Optometrist and Glaucoma Specialist. In his office, I found a degree certificate from the TCU. On curiosity, I asked if he knew Dr. Ernest Couch! To my surprise, he replied to me emotionally that Dr. Couch was his mentor who encouraged and wrote the recommendation letter for the medical schools! Dr. Couch has left us, but his work has left an imprint among us!”

*Nabarun Ghosh, PhD
West Texas A&M University*

“Dr. Ernest Couch was an excellent microscopist, scientist, and teacher. He was an extremely active member of the TSM and a dear friend. He will be missed.”

*Bernd Zechmann, PhD
Baylor University*

IN MEMORIAM DR. ERNEST COUCH



Group photo: Workshop at the 53rd TSM meeting, Denton in 2018



“Ernie was a delightful and helpful member of TSM. I enjoyed interacting with him on the Council, at meetings, and various other events in the 1970’s and 1980’s. His service to our field of EM in the early days was so important. He was a tireless worker, mentor, teacher, contributor and leader. I am glad I knew him.”

Margaret Ann Goldstein, Ph. D.

*TSM charter member, Honorary TSM member, TSM president 1981-1982
Professor Emeritus of Medicine, Professor of Molecular and Cellular Biology
Baylor College of Medicine
Life Member, Clare Hall, University of Cambridge*

“Time’s Arrow leaves in its amplifying wake a sadness in the passing of a beautiful human being...our dear friend, colleague, and respected leader, Dr. Ernest Couch.

Among the world’s greatest academic institutions, we find the frequent juxtaposition of arts and sciences, mediated by both history and the humanities. The great voyages of discovery thereof were commissioned to gain new knowledge and then... by extension... the subsequent dissemination and propagation of this new knowledge...and such was the hallmark of Dr. Couch’s leadership of TSM.

Let truth be the bedrock of new institutions. And what greater allies of truth than the quest for the highest possible resolution, and absolute focus. The excitement of “New Discovery” is always “fair game” but unfortunately, anthropomorphism may introduce truth’s greatest challenges, i.e. subjectivity, and ego... and the latter, I believe, greater challenges of truth, i.e. polarizations, prejudice, and politics. Dr. Couch’s anthropomorphism to TSM is to be celebrated, for he saw beauty in the diversity of its membership, of students, teachers, professors, of all genders of all fields from material sciences and industry, to biology, and medicine and all things in between!

We eulogize with highest laudation the indelible memories of our respected friend and leader, and a life that matters with echoes and heartfelt...resonances. We are so very thankful.”

Charles (Bill) Philpott

TSM charter member, Honorary TSM member, TSM president 1965-1966

Original Research Papers

LIFE SCIENCES
Spring 2021

EXPRESSION OF SEROTONIN RECEPTOR SUBTYPE 3A (5HT3A) ON RAT TRIGEMINAL SENSORY NEURONS

SUKHBIR KAUR, ANGELA LOPEZ-RAMIREZ,
TAYLOR M. HICKMAN, MICHAEL P. HUNTER, DAYNA L. AVERITT*

Department of Biology, Texas Woman's University, Denton, TX 76204, United States

*Corresponding author (daveritt@twu.edu)

Abstract

Serotonin (5-hydroxytryptamine, 5HT) is a neurotransmitter and proinflammatory mediator found largely in the peripheral nervous system where it can initiate pain signaling. 5HT binds a variety of 5HT receptors on sensory nerve endings specialized in detecting noxious stimuli, termed nociceptors. A subset of sensory neurons involved in pain signaling express the transient receptor potential vanilloid 1 ion channel (TRPV1), a pain generator. 5HT can both directly activate sensory neurons and sensitize TRPV1 leading to enhanced nociceptor sensitivity (peripheral sensitization). Previous studies in male rats reported that the 5HT receptor subtype 3A (5HT3A) and TRPV1 are co-expressed on sensory neurons, but it is unknown if 5HT3A and TRPV1 are co-expressed on female sensory neurons. Given that craniofacial pain disorders occur at a 2-3x greater prevalence in women, examining pain mechanisms in female trigeminal sensory neurons that innervate the craniofacial region is critical to advancing craniofacial pain management in women. Here we examined whether (1) 5HT acting via the 5HT3A receptor produces sexually dimorphic orofacial pain behaviors in rats and (2) whether 5HT3A receptor mRNA is expressed in trigeminal sensory neurons, including the TRPV1-expressing subpopulation, and increase pain signaling. We report that 5HT evokes pain behaviors in male and female rats, which was not significantly reduced by antagonism of 5HT3A. We performed *in situ* hybridization to label 5HT3A and TRPV1 mRNA in trigeminal sensory neurons and found distinct cell populations with either 5HT3A mRNA or TRPV1 mRNA in males and females. Further, 5HT3A antagonism failed to reduce pain signaling in cultured trigeminal sensory neurons. These data suggest that the 5HT3A subtype on trigeminal sensory neurons innervating the orofacial soft tissues does not play a significant role in sexually dimorphic craniofacial pain disorders. As previous studies have reported that granisetron reduces masseter muscle pain, 5HT3 may play a role in sex differences in myofascial pain disorders but not in other craniofacial pain disorders.

Keywords: pain; serotonin; 5HT3A receptor; TRPV1 ion channel; RNAScope©

Introduction

Trigeminal pain disorders, like migraine and temporomandibular joint disorder, disproportionately affect women with migraine being 2-3 times more prevalent in women (Berkley, 1997; LeResche et al., 2003). More than half of these women report menstrual-associated migraine in their reproductive years (Granella et al., 1993). Thus, gonadal hormone fluctuations [mainly estrogen (E2)] may be a possible explanation underlying these sex differences in trigeminal pain disorders. In addition, these disorders activate the immune system that release a milieu of pro-inflammatory mediators that can further modulate trigeminal pain signaling. One such proinflammatory and pronociceptive mediator released in the periphery is

serotonin (5HT). 5HT is a neurotransmitter that is also a known peripheral allogen released by cells of the immune system and can act via a variety of excitatory ionotropic and metabotropic 5HT receptors to sensitize peripheral sensory neurons (meaning lower their activation threshold). Of the seven known 5HT receptors (5HT1-7), 5HT3A is an ionotropic receptor that belongs to the nicotinic acetylcholine superfamily of ion channels, whose activation results in the flow of sodium and potassium ions leading to an excitatory current in the sensory neuron (Maricq et al., 1991; Thompson & Lummis, 2007).

5HT is also known to sensitize a cation channel highly expressed in a subpopulation of trigeminal sensory neurons, the transient receptor potential vanilloid 1 (TRPV1) ion

channel. TRPV1 is a thermosensor expressed in small- to medium-sized sensory neurons in the trigeminal ganglia that also acts as a pain generator (Loyd et al., 2013). Activation of TRPV1 by heat ($>42^{\circ}\text{C}$), capsaicin (the 'spicy' chemical in chili peppers), and protons results in an influx of calcium (Ca^{+2}) ions into the sensory neuron. The calcium influx results in the release of additional proinflammatory molecules, largely substance P and calcitonin gene related peptide (CGRP) (Kaur et al., 2018; Vay et al., 2012). 5HT can act through 5HT receptors to sensitize TRPV1 resulting in an increased Ca^{+2} influx and CGRP release (Loyd et al., 2013). We have previously reported that during periods of hormonal fluctuation, 5HT can evoke greater pain behaviors in female rats during the proestrus and estrus phases of the estrous cycle, characterized by rapid fluctuations in estrogen levels. During proestrus, estrogen rapidly rises and peaks and during estrus estrogen rapidly declines. Moreover, treatment with the 5HT_{2A} receptor antagonist, M100907, can attenuate these pain behaviors in both male and female rats suggesting an important role of excitatory 5HT receptors in pain processing (Kaur et al., 2018).

Of the known excitatory 5HT receptors, 5HT_{2A} and 5HT_{3A} have been shown to co-express with TRPV1 in male trigeminal sensory neurons, which provides an anatomical substrate for enhancing pain signaling in the neurons (Kaur et al., 2018). Studies have also reported that blocking the 5HT_{3A} receptor in the central nervous system reduces the sensitization of TRPV1, thus implicating an interaction between 5HT_{3A} and TRPV1 in pain signaling (Kim et al., 2014). Further, 5HT_{3A} antagonists are used as potent antiemetic drugs to block the release of 5HT in the gastrointestinal tract and reduce visceral pain (Theriot et al., 2020). Given that craniofacial pain disorders occur at a 2-3x greater prevalence in women, examining pain mechanisms in female trigeminal sensory neurons that innervate the craniofacial region is critical to advancing craniofacial pain management in women. Here we examined whether (1) 5HT acting via the 5HT_{3A} receptor produces sexually dimorphic orofacial pain behaviors in rats and (2) whether 5HT_{3A} receptor mRNA is expressed in trigeminal sensory neurons, including the TRPV1-expressing subpopulation, and increase pain signaling.

Materials and Methods

Subjects: A total of 16 adult male and 31 adult female Sprague–Dawley rats (200–300 g; Charles River Laboratories, Wilmington, MA) were used in the experiments. Rats were separated by sex and pair-housed in a 12:12-h light: dark cycle with ad libitum food and water access. All studies were approved by the Texas Woman's University Institutional Animal Care and Use Committee and conform to federal guidelines and guidelines of the Committee for Research and Ethical Issues of the International Association for the Study of Pain. This study was conducted in strict compliance with the Animal Welfare Act, implementing Animal Welfare Regulations, and the principles of the Guide for the Care and Use of Laboratory Animals.

Vaginal cytology: Vaginal lavages were performed between 9:00 AM to 11:00 AM at 24-h intervals beginning 2 weeks (at least two consecutive cycles; 10 days) before testing to confirm that all female rats were cycling normally. Daily records were maintained on the stages of their cycle through the day of experimental testing and tissue collection. Proestrus was identified as a predominance of nucleated epithelial cells and estrus was identified as a predominance of cornified epithelial cells. Diestrus 1 (or metestrus) was differentiated from diestrus 2 (or diestrus) by the presence of leukocytes (Becker et al., 2005; Loyd & Murphy, 2008; McLean et al., 2012).

Ovariectomy: A subset of female rats were deeply gas anesthetized (3% induction; 2.5% maintenance) by inhalation of Isothesia (isoflurane, USP, Henry Schein Animal Health, Dublin, OH) and a single incision was made across the abdomen. The abdominal muscle was opened and the ovary bundles were ligated with 4-O silk sutures, excised, and removed. The fascia was closed with 5-O silk suture and the skin was closed with Vicryl sutures to prevent wicking. Rats were allowed 2 weeks for recovery and ovarian hormone dissipation. Trigeminal ganglia were removed from these animals following the 2-week recovery period using methodology described under the cell culture methodology section.

Behavior Testing: Square-shaped plexiglass boxes (30 x 30 x 30 cm) with mirrored sides were used to observe orofacial nocifensive (pain-provoked) behaviors. Rats were acclimated to the behavior testing apparatus 24 hours prior to testing. On the day of testing, rats were placed in the individual boxes immediately post-injection and nocifensive behavior was recorded with a video camera for a 30-min time period. The videos were manually quantified using iMovie software (Apple Inc., Mac OS) by counting the number of forelimb swipes over the injection site in 6 min bouts over an 18 min period and reported as a measure of spontaneous nocifensive behavior. Data was counted by an independent observer blind to the experimental condition.

Adult intact male and cycling female rats in either proestrus or estrus received an unilateral intradermal injection of the selective 5HT_{3A} antagonist granisetron (1 μM ; 0.1 nmol / 100 μL ; Sigma-Aldrich) (Loyd, Chen, et al., 2012) or saline vehicle control (0.9%; 100 μL) into the vibrissal pad ($n = 7 - 8$ per sex and per treatment group). Fifteen-minutes after the pre-treatment, female rats received an injection of 5HT (3 μg / 50 μL) and the male rats received an injection of 5HT combined with capsaicin (3 μg 5HT + 1 μg CAP / 50 μL) at the same site. The male rats received the addition of capsaicin because our previous studies indicate 3 μg 5HT does not induce orofacial nocifensive behavior, while in females 3 μg 5HT produces significant orofacial nocifensive behavior. Immediately following the 5HT injection, orofacial nocifensive behavior were recorded and counted as described above.

In situ hybridization: Trigeminal ganglia were bilaterally extracted from males and cycling female rats two weeks following orofacial behavior testing and immediately frozen

on dry ice. The tissues were stored at -80° until processing. The ganglia ($n=2$ / animal) were embedded in Tissue-Tek Optimal Cutting Temperature (O.C.T) compound (Sakura Finetek USA) and cut into $30\ \mu\text{m}$ sections on a Leica Cryostat CM3050 at -20° . The slides were then stored at -80° until further processing. For in situ hybridization, the RNAScope[®] Fluorescent Multiplex Assay was performed according to the manufacturer's specifications (ACD Biotechne) with optimizations performed for TG tissue. Briefly, slides were fixed in 4% paraformaldehyde, sequentially dehydrated in 50% ethanol, 70% ethanol, and 100% ethanol and stored at -20° overnight. The next day, slides were air-dried and incubated at 60° and a hydrophobic barrier was drawn using an ImmEdge Hydrophobic Barrier Pen (Vector Laboratories). Following a hydrogen peroxide and protease IV treatment, the slides were treated with either experimental probes (50:1 dilution; Table 1) or control probes and incubated at 40° for 2 hours. Slides were washed in buffer and amplification steps were performed with AMP-1, AMP-2, and AMP-3 (AMP indicates proprietary signal amplification molecules; ACD Biotechne), then slides were sequentially treated with OPAL fluorophores (Table 1; Akoya Biosciences). Excess liquid was carefully drained from the slides and 1 - 2 drops of Prolong Gold antifade mounting medium (Fisher Scientific) and slides were cover slipped and air-dried overnight at room temperature. The slides were imaged using a Zeiss LSM 900 confocal microscope. Zeiss ZEN software was used to view and capture the images at 40X. The staining intensity was filtered by applying a laser power based on the control slides (Laser power - 570nm: 0.2%, 520nm: 1%) to remove low intensity pixels that represent nonspecific/background staining. All images were saved in tiff format for presentation.

Probe	Target	Channel	Fluorophore	Image Color	Working Dilution
Htr-3a	Serotonin receptor subtype 3A (5HT _{3A}) mRNA	C1	OPAL 570	Magenta puncta	1:1500
Trpv1	Transient Receptor Potential Vanilloid 1 ion channel (TRPV1) mRNA	C2	OPAL 520	Green puncta	1:1000

Table 1: Specifications of the RNAScope[™] Fluorescent Multiplex Assay for in situ hybridization.

Primary culture of trigeminal ganglia neurons: Trigeminal ganglia ($n=4$ rats per 24-well plate run in triplicate) were extracted from adult ovariectomized female rats (~ 200 g) immediately following decapitation under brief gas anesthesia (3% isoflurane). Primary neuron cultures were prepared using previously described methods (Lloyd et al., 2011). Briefly, trigeminal ganglia were suspended in Hank's balanced salt solution (HBSS) on ice and gently washed three times. After dissociation with collagenase (5%, Worthington Biochemical Corp) and trypsin (1%, Sigma-Aldrich) at 37°C , the cells were suspended in Dulbecco's modified Eagle's medium (DMEM; Invitrogen) containing 10% fetal bovine serum, 1X glutamine (Gibco), 1X penicillin-streptomycin (Gibco), nerve growth factor (100

ng/mL; Harlan, Indianapolis, IN), and treated with mitotic inhibitors 5-fluoro-2'-deoxyuridine ($3\ \mu\text{g}/\text{mL}$; Invitrogen) and uridine ($7\ \mu\text{L}/\text{mL}$; Sigma-Aldrich). Cells were then lightly dissociated using a 20-gauge followed by a 23-gauge needle and then applied to 24-well poly-D-lysine-coated plates (Corning) and maintained in an incubator at 37°C and 5% CO_2 .

CGRP Release Assay: Primary cultures of trigeminal sensory neurons were grown and maintained for 5 days prior to running the CGRP release assay. The assay was performed using a protocol previously described (Lloyd et al., 2011). Briefly, cultures were washed twice with $300\ \mu\text{L}$ HBSS. Cells were then incubated in HBSS for 15 minutes and supernatant was collected for measurement of basal CGRP release from the neurons. The same cultures were then pretreated row-wise with either granisetron (100 nM) or 17β -estradiol (E2; 50 nM), followed by 5HT (100 μM) for 15 minutes and supernatant was collected for measurement of treatment-evoked CGRP release. Then cells in all the rows were stimulated with capsaicin (50 nM) to trigger CGRP release and supernatant was collected for measurement of the effects of treatment on capsaicin-evoked CGRP release. CGRP in the superfusate was detected using a rat-specific CGRP ELISA (Cayman Chemical) and quantified using a Biotek ELx808 absorbance reader (Biotek). All experiments were conducted in duplicate with $n = 6$ wells per treatment group for a total of approximately 12 wells per group.

Data analysis: All data were analyzed and graphed with GraphPad Prism software version 9.0.0 (GraphPad, San Diego, CA). Orofacial nocifensive behavior and CGRP release data were expressed as mean \pm standard error of the mean (SEM) and were analyzed by two-way ANOVA. Grubb's test was used to exclude a single outlier within an experimental group if present and Bonferroni's correction was used to calculate a priori pairwise comparisons.

Results

Granisetron does not significantly attenuate 5HT-evoked orofacial nocifensive behaviors in male or female rats

Since 5HT_{3A} is expressed in the trigeminal ganglia and is an excitatory ion channel, we first determined whether 5HT evokes nocifensive behaviors via the 5HT_{3A} receptor in male and female rats. 5HT alone evoked significant orofacial pain behaviors (saline pre-treatment group) within 10 minutes of 5HT injection in female rats and within 10 minutes of injection of 5HT with capsaicin (5HT+CAP) in male rats [$p < 0.05$]. Local pre-treatment with the selective 5HT_{3A} receptor antagonist, granisetron, 15 minutes prior to either 5HT injection in females or 5HT+CAP injection in males did not significantly attenuate orofacial nocifensive behaviors (Figure 1A and 1B) [$p > 0.05$].

5HT_{3A} receptor mRNA and TRPV1 ion channel mRNA are co-expressed in male and female trigeminal sensory neurons

We then performed in situ hybridization to determine whether 5HT_{3A} receptor mRNA co-expresses with TRPV1 ion channel mRNA in the trigeminal sensory neurons of

the trigeminal ganglia of male and female rats. We report 5HT_{3A} mRNA expression in distinct small and medium diameter neurons in the trigeminal sensory neurons of the trigeminal ganglia of males and cycling female rats (Figure 2; magenta fluorescent puncta). TRPV1 ion channel mRNA was also observed in small and medium diameter neurons in the trigeminal sensory neurons of the trigeminal ganglia of males and cycling female rats (green fluorescent puncta). In both males and females, and across the estrous cycle, there was a subset of the sensory neuron population that co-expressed 5HT_{3A} receptor mRNA and TRPV1 ion channel mRNA (Figure 2; white fluorescent puncta).

Granisetron does not significantly attenuate proinflammatory peptidergic activity in cultured trigeminal sensory neurons

As the proinflammatory peptide CGRP is released from sensory neurons when TRPV1 is activated, quantification of CGRP is a measure of nociceptive peptidergic activity in sensory neurons. Here we tested whether blocking the 5HT_{3A} receptor attenuates 5HT- and/or capsaicin-evoked CGRP release from cultured trigeminal sensory neurons extracted from ovariectomized female rats.

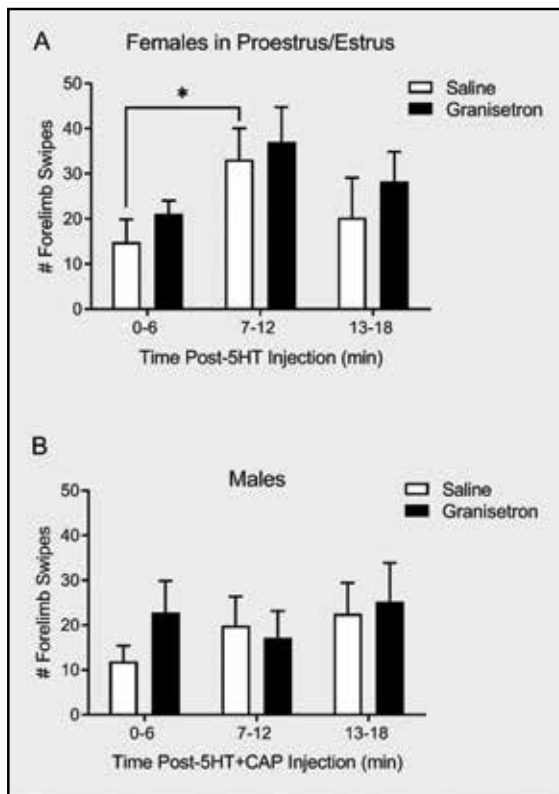


Figure 1. Effects of granisetron on female and male rats. Bar graphs illustrate the effects of saline pre-treatment (open bars) and granisetron pre-treatment (closed bars) on serotonin (5HT) alone in female rats (A) or 5HT with capsaicin (5HT+CAP) in male rats (B) on orofacial nociceptive behaviors recorded as the number of forelimb swipes from 0-18 minutes following injection into the vibrissal (cheek) pad. Asterisks indicate significant effect of 5HT on pain behaviors compared to vehicle treatment ($p < 0.05$). There was no significant effect of granisetron on pain behaviors ($p > 0.05$).

When the neurons were treated with 5HT, E2, or granisetron alone (pretreatment) there was no effect on CGRP release (Figure 3) [$p > 0.05$]. Capsaicin evoked significant CGRP release that was enhanced by 5HT and E2 (Figure 3 grey bars) [$p < 0.05$]. CGRP release was not attenuated by pretreatment with the 5HT_{3A} antagonist granisetron [$p > 0.05$].

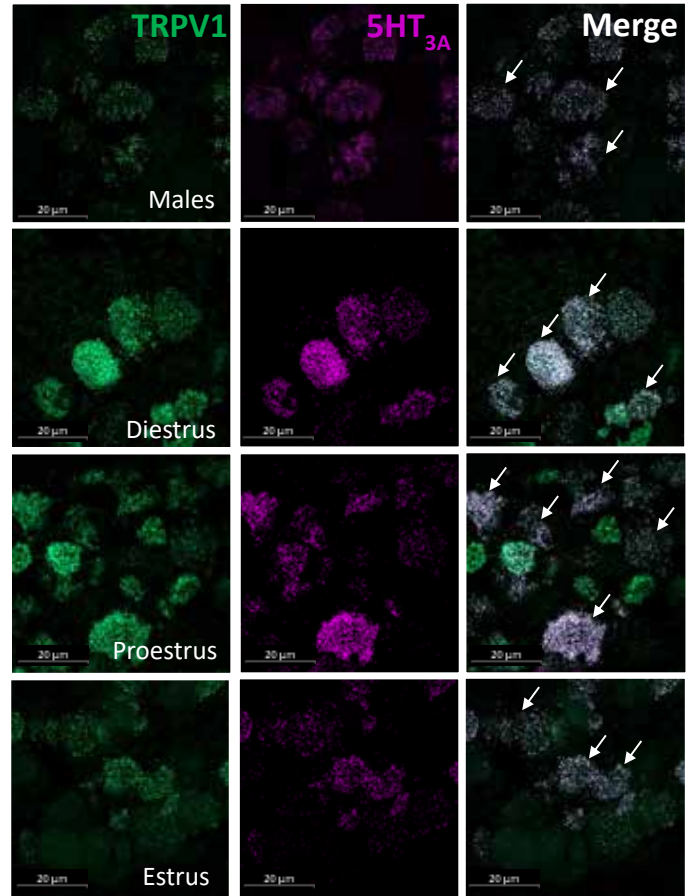


Figure 2: Expression of 5HT_{3A} receptor and TRPV1 ion channel in trigeminal ganglia. Representative images of the expression of 5HT_{3A} receptor mRNA (magenta) and TRPV1 ion channel mRNA (green) in the trigeminal ganglia of male and cycling female rats across the three stages of the estrous cycle [diestrus, proestrus (P), and estrus (E)]. The first column illustrates TRPV1 ion channel mRNA expression, the second column illustrates 5HT_{3A} receptor mRNA expression, and the third column is an overlay of 5HT_{3A} receptor mRNA and TRPV1 ion channel mRNA. Arrows indicate sensory neurons co-expressing 5HT_{3A} receptor mRNA and TRPV1 ion channel mRNA (white).

Discussion

Trigeminal pain disorders are more prevalent and severe in duration and intensity in women than men. Understanding the role of excitatory 5HT receptors in peripheral pain processing is important to the development of more effective, and even sex-specific, therapeutics. We have previously reported that 5HT-evoked pain behaviors are increased during phases of the rodent estrous cycle when gonadal hormones are greatly fluctuating and that blocking the Gq-coupled 5HT_{2A} receptor attenuates E2-

enhanced pain behaviors (Kaur et al., 2018). In this study we report that (1) blocking the 5HT3A receptor does not attenuate 5HT-evoked orofacial nocifensive pain behaviors, (2) 5HT3A mRNA co-expresses with TRPV1 on male and female trigeminal sensory neurons, and (3) blocking the 5HT3A receptor does not attenuate capsaicin-evoked CGRP release from cultured trigeminal sensory neurons.

Previous studies have reported that blocking the excitatory 5HT2A and 5HT3A receptors attenuates pain signaling in male cultured trigeminal sensory neurons (Loyd, Chen, et al., 2012; Loyd et al., 2013; Loyd et al., 2011). In support, 5HT2 and 5HT4 receptor antagonists attenuate 5HT-potentiated current in mouse DRG neurons (Sugiura et al., 2004). In the present study, we report that orofacial pain behaviors were not attenuated in the presence of granisetron. These data indicate that the ionotropic 5HT3 receptor is not necessary for 5HT-evoked pain in the vibrissal pad. It is likely that the 5HT3 receptor is involved in generating pain in male and female rats, but antagonism of only the 5HT3 receptor is not sufficient to reduce orofacial pain in male or female rats. Rather, the involvement of the other excitatory G-protein coupled 5HT receptors are key to orofacial pain, such as the 5HT2A receptor. Interestingly, 5HT3 receptors are upregulated in the masseter muscle of women with myofascial pain compared to healthy controls indicating that 5HT3 receptors may be more involved in pain processing in pathological trigeminal nociceptors innervating painful muscle rather than other trigeminal nociceptors (Christidis et al., 2014). In support, granisetron significantly reduces muscle pain, but not thermal pain, in men and women (Ernberg et al., 2020; Louca et al., 2013).

Studies have also reported that 5HT1A, 5HT1D, 5HT2A and 5HT3A receptors co-localize with TRPV1 on male trigeminal sensory neurons (Loyd et al., 2011). To date, no studies had examined whether 5HT receptors are co-expressed with the TRPV1 ion channel in female trigeminal sensory neurons. In the present study, we report that 5HT3A mRNA co-expresses with TRPV1 ion channels on male and female trigeminal sensory neurons. The soma of nociceptors housed in the trigeminal ganglia are typically small- to medium-sized in diameter (~15-35 μ m). 5HT3A receptor mRNA and TRPV1 ion channel mRNA were expressed in the small- to medium-sized sensory neuron population. As the TRPV1 ion channel in a major pain generator, the population of sensory neurons that express TRPV1 are classified as nociceptors, though not all nociceptors express TRPV1 ion channels. Thus, our data provide evidence that 5HT3A receptors are expressed by a subpopulation of nociceptors in the trigeminal ganglia. Regions with white fluorescent puncta indicating a cell expressing both TRPV1 mRNA and 5HT3A receptor mRNA was observed in both sexes and across the four stages of estrous cycle. While 5HT3A receptors appear to be localized on nociceptors in the trigeminal ganglia, our behavioral data indicate that blocking only the peripheral 5HT3A receptors is not sufficient to reduce orofacial pain. We are currently examining whether 5HT2A receptor

mRNA is co-expressed in the TRPV1 population of trigeminal nociceptors and whether blocking peripheral 5HT2A receptors is sufficient to reduce orofacial pain in female rats.

CGRP release is a measure of nociceptive peptidergic activity in sensory neurons and studies have correlated high CGRP release to worsened migraine symptoms in women (Goadsby et al., 1990; Hansen et al., 2010). Moreover, studies have reported that 5HT enhances capsaicin-evoked CGRP release from rat sensory neurons (Loyd et al. 2011) and female human tooth pulp (Loyd, Sun, et al., 2012). In concurrence with the in vivo arm of this study, our in vitro examination of the effects of granisetron on capsaicin-evoked CGRP release found that blocking the 5HT3 receptor does not alter 5HT-evoked pain signaling.

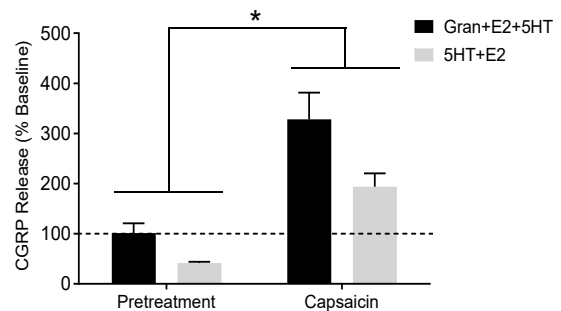


Figure 3: Effects of granisetron on cGCRP release. Primary cultures pretreated with either the selective 5HT3 receptor antagonist granisetron (black pretreatment bar) or vehicle (grey pretreatment bar) prior to treatment with serotonin (5HT) and 17 β -estradiol (E2) and stimulation with the TRPV1 agonist capsaicin. Asterisks indicate significant effect of 5HT+E2 on CGRP release as compared to vehicle ($p < 0.05$). There was no significant effect of granisetron on the enhanced CGRP release ($p > 0.05$).

Conclusion

Overall, the present study indicates that, while the ionotropic 5HT3 receptor may be involved in 5HT-evoked orofacial pain in female rats, selective antagonism of the 5HT3 receptor with granisetron is not sufficient to reduce 5HT-evoked orofacial pain and thus not involved in the sexually dimorphic effects of peripheral 5HT on orofacial pain. Thus, it is more likely that a metabotropic 5HT receptor needs to be blocked to reduce 5HT-evoked orofacial pain in female rats. Further, this study is the first to report that 5HT3A receptor mRNA is co-expressed with TRPV1 ion channel mRNA on both male and female trigeminal sensory neurons. Our data leads us to speculate that drugs targeting the peripheral 5HT3 receptor may not be sufficient to reduce trigeminal pain conditions not of muscle origin, such as migraine, in both men and women. Our current studies are now focused on the metabotropic 5HT receptors known to be localized to the trigeminal ganglia to determine whether targeting a different excitatory 5HT receptor may reduce orofacial pain.

Funding

This work was funded by a Texas Society of Microscopy Small Grant awarded to SK, a Texas Woman's University Research Enhancement Grant to DLA, and a National Institute of Dental and Craniofacial Research grant DE026749 to DLA.

References

- Becker, J. B., Arnold, A. P., Berkley, K. J., Blaustein, J. D., Eckel, L. A., Hampson, E., Herman, J. P., Marts, S., Sadee, W., Steiner, M., Taylor, J., & Young, E. (2005). Strategies and methods for research on sex differences in brain and behavior. *Endocrinology*, 146(4), 1650-1673. <https://doi.org/10.1210/en.2004-1142>
- Berkley, K. J. (1997). Sex differences in pain. *Behav Brain Sci*, 20(3), 371-380; discussion 435-513. <https://doi.org/10.1017/s0140525x97221485>
- Christidis, N., Kang, I., Cairns, B. E., Kumar, U., Dong, X., Rosén, A., Kopp, S., & Ernberg, M. (2014). Expression of 5-HT₃ receptors and TTX resistant sodium channels (Na(V)1.8) on muscle nerve fibers in pain-free humans and patients with chronic myofascial temporomandibular disorders. *The Journal of Headache and Pain*, 15(1), 63-63. <https://doi.org/10.1186/1129-2377-15-63>
- Ernberg, M., Wieslander Fältmars, A., Hajizadeh Kopayeh, M., Arzt Wallén, S., Cankalp, T., & Christidis, N. (2020). The Effect of Granisetron on Sensory Detection and Pain Thresholds in Facial Skin of Healthy Young Males [Original Research]. *Frontiers in Neurology*, 11(237). <https://doi.org/10.3389/fneur.2020.00237>
- Goadsby, P. J., Edvinsson, L., & Ekman, R. (1990). Vasoactive peptide release in the extracerebral circulation of humans during migraine headache. *Ann Neurol*, 28(2), 183-187. <https://doi.org/10.1002/ana.410280213>
- Granello, F., Sances, G., Zanferrari, C., Costa, A., Martignoni, E., & Manzoni, G. C. (1993). Migraine without aura and reproductive life events: a clinical epidemiological study in 1300 women. *Headache*, 33(7), 385-389. <https://doi.org/10.1111/j.1526-4610.1993.hed3307385.x>
- Hansen, J. M., Hauge, A. W., Olesen, J., & Ashina, M. (2010). Calcitonin gene-related peptide triggers migraine-like attacks in patients with migraine with aura. *Cephalalgia*, 30(10), 1179-1186. <https://doi.org/10.1177/0333102410368444>
- Kaur, S., Benton, W. L., Tongkhuya, S. A., Lopez, C. M. C., Uphouse, L., & Averitt, D. L. (2018). Sex Differences and Estrous Cycle Effects of Peripheral Serotonin-Evoked Rodent Pain Behaviors. *Neuroscience*, 384, 87-100. <https://doi.org/10.1016/j.neuroscience.2018.05.017>
- Kim, Y. S., Chu, Y., Han, L., Li, M., Li, Z., LaVinka, P. C., Sun, S., Tang, Z., Park, K., Caterina, M. J., Ren, K., Dubner, R., Wei, F., & Dong, X. (2014). Central terminal sensitization of TRPV1 by descending serotonergic facilitation modulates chronic pain. *Neuron*, 81(4), 873-887. <https://doi.org/10.1016/j.neuron.2013.12.011>
- LeResche, L., Mancl, L., Sherman, J. J., Gandara, B., & Dworkin, S. F. (2003). Changes in temporomandibular pain and other symptoms across the menstrual cycle. *Pain*, 106(3), 253-261. <https://doi.org/10.1016/j.pain.2003.06.001>
- Louca, S., Ernberg, M., & Christidis, N. (2013). Influence of intramuscular granisetron on experimentally induced muscle pain by acidic saline. *J Oral Rehabil*, 40(6), 403-412. <https://doi.org/10.1111/joor.12046>
- Loyd, D. R., Chen, P. B., & Hargreaves, K. M. (2012). Anti-hyperalgesic effects of anti-serotonergic compounds on serotonin- and capsaicin-evoked thermal hyperalgesia in the rat. *Neuroscience*, 203, 207-215. <https://doi.org/10.1016/j.neuroscience.2011.12.019>
- Loyd, D. R., Henry, M. A., & Hargreaves, K. M. (2013). Serotonergic neuromodulation of peripheral nociceptors. *Semin Cell Dev Biol*, 24(1), 51-57. <https://doi.org/10.1016/j.semcdb.2012.09.002>
- Loyd, D. R., & Murphy, A. Z. (2008). Androgen and estrogen (alpha) receptor localization on periaqueductal gray neurons projecting to the rostral ventromedial medulla in the male and female rat. *J Chem Neuroanat*, 36(3-4), 216-226. <https://doi.org/10.1016/j.jchemneu.2008.08.001>
- Loyd, D. R., Sun, X. X., Locke, E. E., Salas, M. M., & Hargreaves, K. M. (2012). Sex differences in serotonin enhancement of capsaicin-evoked calcitonin gene-related peptide release from human dental pulp. *Pain*, 153(10), 2061-2067. <https://doi.org/10.1016/j.pain.2012.06.018>
- Loyd, D. R., Weiss, G., Henry, M. A., & Hargreaves, K. M. (2011). Serotonin increases the functional activity of capsaicin-sensitive rat trigeminal nociceptors via peripheral serotonin receptors. *Pain*, 152(10), 2267-2276. <https://doi.org/10.1016/j.pain.2011.06.002>
- Maricq, A. V., Peterson, A. S., Brake, A. J., Myers, R. M., & Julius, D. (1991). Primary structure and functional expression of the 5HT₃ receptor, a serotonin-gated ion channel. *Science*, 254(5030), 432-437. <https://doi.org/10.1126/science.1718042>
- McLean, A. C., Valenzuela, N., Fai, S., & Bennett, S. A. (2012). Performing vaginal lavage, crystal violet staining, and vaginal cytological evaluation for mouse estrous cycle staging identification. *J Vis Exp*(67), e4389. <https://doi.org/10.3791/4389>
- Sugiura, T., Bielefeldt, K., & Gebhart, G. F. (2004). TRPV1 function in mouse colon sensory neurons is enhanced by metabotropic 5-hydroxytryptamine receptor activation. *Journal of Neuroscience*, 24(43), 9521-9530. <https://doi.org/10.1523/Jneurosci.2639-04.2004>
- Theriot, J., Wermuth, H. R., & Ashurst, J. V. (2020). Antiemetic Serotonin-5-HT₃ Receptor Blockers. In *StatPearls*. <https://www.ncbi.nlm.nih.gov/pubmed/30020690>
- Thompson, A. J., & Lummis, S. C. (2007). The 5-HT₃ receptor as a therapeutic target. *Expert Opin Ther Targets*, 11(4), 527-540. <https://doi.org/10.1517/14728222.11.4.527>
- Vay, L., Gu, C., & McNaughton, P. A. (2012). The thermo-TRP ion channel family: properties and therapeutic implications. *Br J Pharmacol*, 165(4), 787-801. <https://doi.org/10.1111/j.1476-5381.2011.01601.x>

COLORADO TICK FEVER VIRUS-INDUCED ULTRASTRUCTURAL CHANGES IN HUMAN AND MONKEY CELL LINES

SARAH OWEN¹, CAITLYN GAFFNEY¹, JUDY A. KING², RAJESH P. BALARAMAN¹, AND JEREMY BECHELLI^{1*}

¹ Department of Biological Sciences, Sam Houston State University, Huntsville, Texas 77340

² Department of Pathology and Translational Pathobiology, Louisiana State University Health, Shreveport, Louisiana, USA.

*Corresponding author (jrb138@shsu.edu)

Abstract

Colorado Tick Fever Virus (CTFV) is the type species of the genus *Coltivirus* of the family *Reoviridae*, and the causative agent of Colorado tick fever (CTF). CTF is characterized by a biphasic fever lasting up to 10 days, flulike syndromes including chills, headache, and myalgia, as well as retroorbital pain and photophobia. Up to 10% of pediatric patients infected with CTFV can develop severe manifestations that affect the central nervous system, such as meningitis or encephalitis, hemorrhagic fever, and death. Although this disease can be severe, no drug therapy exists for CTF, and there is little information on the mechanisms underlying CTFV induced pathology during infection. This study shows that CTFV induces specific ultrastructural changes in monkey cells (Vero) that are not observed in human dermal endothelial cells (HMEC-1). We describe CTFV-induced fibers commonly seen in Vero cells that are not present in HMEC-1 endothelium, as well as ultrastructural changes associated with both cell types. While this work is currently descriptive, ongoing and future work will explore viral-induced fiber function and protein composition.

Keywords: Colorado tick fever virus, transmission electron microscopy, intra-nuclear and cytoplasmic fibrils, morphology changes, Vero and HMEC-1 cell lines.

Introduction

Colorado tick fever virus (CTFV) belongs to the genus *Coltivirus* of the *Reoviridae* family and is the causative agent of Colorado tick fever (CTF), a tick-borne disease in North America transmitted by *Dermacentor andersoni* (Florio et al. 1950). CTF is generally a mild and self-limiting disease characterized by biphasic fever, headache, myalgia, fatigue, and some may develop a petechial rash (Goodpasture et al., 1978). However, serious clinical manifestations affecting the central nervous system can develop in 5-10% of pediatric patients, including aseptic meningitis, meningoencephalitis, or encephalitis (Emmons, 1988; Krauss et al., 2004). Hemorrhagic fever, pericarditis, myocarditis, and orchitis have also been observed, and disease severity results in hospitalization of approximately 20% of patients (Attoui et al., 2005). No drug treatment currently exists to address the illness, and limited research findings related to the mechanisms underlying CTFV induced pathology have been conducted. Previous studies have shown that CFTV replicates in erythroblasts, reticulocytes, human bone marrow CD34+, and hematopoietic progenitor cells (Oshiro et al., 1978; Philipp et al., 1993). However, the effect and morphological changes due to CFTV infection in other cell types are not well described.

Transmission electron microscopy (TEM) is an advanced imaging technique that uses an electron beam to examine the ultrastructural morphology of viral particles (Roingard et al., 2019) and morphological changes in virus-infected cells. TEM allows for the visualization of different stages of entry, replication, and progression of viral particles and the resulting pathology in the host (Goldsmith

and Miller, 2009). Early TEM studies on CTFV have shown intracytoplasmic and intranuclear fibrillar structures in baby hamster kidney cells (BHK21), KB cells, hematopoietic progenitor cells (KG-1A), human erythroblast cells (HEL), and primary human bone marrow cells infected with CTFV (Murphy et al., 1968; Philipp et al., 1993).

This study investigated the morphological changes induced by CFTV in two cell lines, Vero and human microvascular endothelial cells (HMEC-1), using TEM. CTFV infected Vero cells have been reported to induce cytopathic effect and are frequently used to propagate CTFV (Karabatsos et al., 1987). The HMEC-1 cell line was used for two reasons; 1. it serves as a model for CTF hemorrhagic manifestations (Attoui et al., 2005), and 2. human dermal endothelial cells are likely one of the first cell types to interact with the virus following its transmission via a tick bite. Here, we have shown the presence and characteristics of intra-nuclear and cytoplasmic fibrils in selected cell lines and the morphological changes resulting from the CFTV infection in Vero and HMEC-1 cells. The current study provides evidence for future studies investigating the role of intra-nuclear (NF) and cytoplasmic fibrils (CF) in cytoskeletal architecture, cell apoptosis, and their existence in various cell types.

Materials and Methods

Virus and Cell culture: CTFV (Florio strain) was obtained from the World Reference Center for Emerging Viruses and Arboviruses (WRCEVA) at the University of Texas Medical Branch, Galveston, TX. This virus stock was propagated in Vero (ATCC CCL-81) cells and quantified by plaque assay.

Vero cells were cultivated in DMEM supplemented with 10% heat-inactivated fetal bovine serum. Human monocytic leukemia cells (THP-1; ATCC TIB-202) were propagated in RPMI 1640 with 2 mM L-glutamine, 10 mM HEPES, 1 mM sodium pyruvate, 4500 mg/L glucose, and 10% fetal bovine serum. HMEC-1 cells (ATCC CRL-3243) were cultured in MCDB 131 medium (Gibco, Grand Island, NY) supplemented with 10 mM L-glutamine, 10 ng/mL mouse epidermal growth factor, 1 µg/mL hydrocortisone, and 10% heat-inactivated fetal bovine serum. All cell cultures were maintained at 37°C in a 5% CO₂ atmosphere.

CTFV infection of human and monkey cells: Human endothelial cells, HMEC-1, and monkey Vero cells were plated as monolayers in 6-well culture plates. All cells were infected with the Florio strain of CTFV at a dose of 1.0 multiplicity of infection (MOI), and the plates were incubated at 37°C in a 5% CO₂ atmosphere for 24 hours. As controls, cells were incubated with culture supernatants from uninfected Vero cells (mock-infected controls). Experiments were completed with three independent sets of biological replicates and representative micrographs were chosen for publication.

TEM Imaging: Ultrathin sections were prepared for TEM imaging (Schrand et al., 2010; Spurr, 1969). Briefly, the CTFV-infected and uninfected cells were fixed with 3% paraformaldehyde and 0.35% glutaraldehyde in 0.1M cacodylate buffer (pH 7.4). After 3 hours, the monolayers were gently peeled off from the surface using cell scrapers and cacodylate buffer. The cells were pelleted at 1200 rpm for 5 min and washed with 0.1M cacodylate buffer (two times for 30 min each). The cell pellets were then postfixed with 2% osmium tetroxide in 0.1 M cacodylate buffer (pH 7.4) for 90 minutes. Further, the pellet was subjected to a series of ethanol dehydration (25%, 50%, 75%, 90%, and 100%) each 30 min. The dehydrated pellet was treated with propylene oxide and embedded in Spurr resin medium (25%, 50%, and 80% for one hour each and 100% overnight on a rotator). After 24 hours, the specimens were transferred into beam capsules filled with 100% Spurr resin and polymerized at 70°C for 36 hours. The resin was cut into 50-100 nm sections using an ultramicrotome (Leica microsystems UC7) and stained with freshly prepared 2% aqueous uranyl acetate for 20 min and lead citrate for 5 min. The stained sections were imaged at 60kV high contrast using Hitachi TEM 7500 (Okinawa, Japan). All chemicals were purchased from Electron Microscopy Sciences (Hatfield, PA), unless mentioned. The images were further analyzed using Image J software (Schneider et al., 2012).

Results

Vero cells

TEM images of uninfected Vero cells (Figure 1A) revealed well-preserved and intact cellular membranes with typical cell morphology characteristics such as a prominent nucleolus in the nucleus, standard chromatin structure, no significant vacuolization, and minimal (irregular) surface projections. Within 24 hours of CTFV infection

(Figure 1B), numerous bulbous surface projections were seen in infected cells, indicating early stages of apoptosis onset. Several cells displayed clear indications of cell death involving heavily vacuolated cytoplasm, remnants of damaged mitochondria (top insert in Figure 1B), as well as granular matrixes indicated with an asterisk (Figure 1B bottom insert). TEM showed virus particles (~70+3 nm in diameter) within the cellular cytoplasm in Figure 1C (insert showing a higher magnification of CFTV). Infected cells showed prominent dilated ER (Figure 1C) and dilation of the nuclear membrane (Figure 1D), represented by black arrow heads. Infected Vero cells (Figure 1D) had intra-nuclear fibrils and cytoplasmic fibrils previously observed in specific cell types infected with CFTV (Murphy et al., 1968; Oshiro et al., 1978; Oshiro and Emmons, 1968; Philipp et al., 1993). Nuclear fibrils measure 0.73 ± 0.29 µm long and cytoplasmic fibrils average 0.37 ± 0.13 µm long. Interestingly, intra-nuclear fibrils tend to remain separated in low numbers, while cytoplasmic fibrils aggregate into clusters with neighboring fibers (Figure 1E). Higher magnification of cytoplasmic fibrils showed a striped and unstriped pattern in the images (Figure 1F). Other characteristics of mitochondrial disruption with loss of cristae and swelling (top insert in Figure 1B), dilated endoplasmic reticulum (Figure 1C), plasma membrane breakdown (Figure 1D), dissolved cytosol (Figure 1D), and dilation of the nuclear membrane (Figure 1D) were seen in a subset of infected cells.

HMEC-1 Cells

TEM imaging of uninfected cells displayed excellent preservation of cellular structures, including numerous mitochondria, prominent nucleolus in the nucleus, and multiple thin surface projections (Figure 2A). HMEC-1 cells infected with CTFV had displayed large bulbous surface projections (Figure 2B) and numerous vacuoles (Figure 2C) in the cytoplasmic region of infected cells compared to uninfected HMEC-1 cells (Figure 2A). We primarily observed virions of ~70+3 nm (in diameter) diffused throughout the cytoplasm of infected cells; however, CTFV virions were also detected in separate large virion-containing vacuoles (VCVs) shown in Figure 2C (insert showing a higher magnification of vacuoles with viral particles). Infected HMEC-1 cells appeared to have alterations of the cristae in the mitochondria, severely swollen mitochondria with breakdown of the cristae, and disruption in the mitochondrial membrane with a loss of density in the matrix (Figure 2D-F) and numerous granular matrices. We could not locate any viral-induced intra-nuclear or cytoplasmic fibrils in any CTFV infected-HMEC-1 cells (Figure 2B-F).

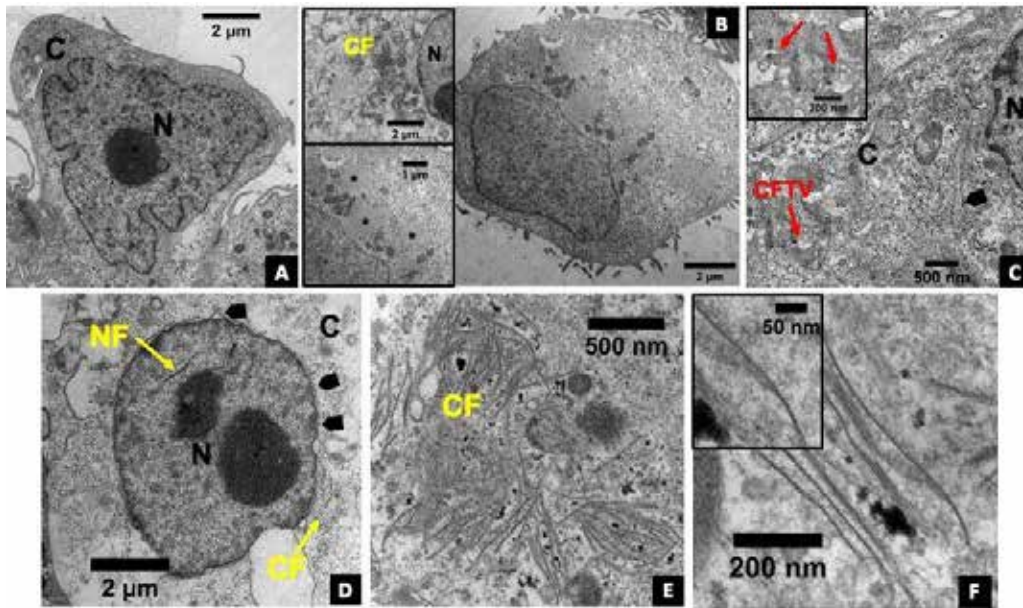


Figure 1. TEM micrographs of CTFV-induced morphological changes in Vero cells. (A) uninfected Vero cell (B) infected Vero cell at 24 hours post-infection showing bulbous surface formation (insert showing numerous cytoplasmic fibrils (CF) and swollen mitochondria, as well as granular matrices labeled with an asterisk). (C) CTFV in the cytoplasm (red arrows) of infected Vero cells (insert shows high magnification of viral particles) and dilated endoplasmic reticulum (black arrowhead). (D) infected Vero cells showing the presence of intra-nuclear and cytoplasmic fibrils (yellow arrows) and dilation of the nuclear membrane (black arrowheads). (E) clusters of cytoplasmic fibers (labeled CF), and (F) striped and unstriped pattern of the cytoplasmic fibrils (insert shows a high magnification of the fibrils).

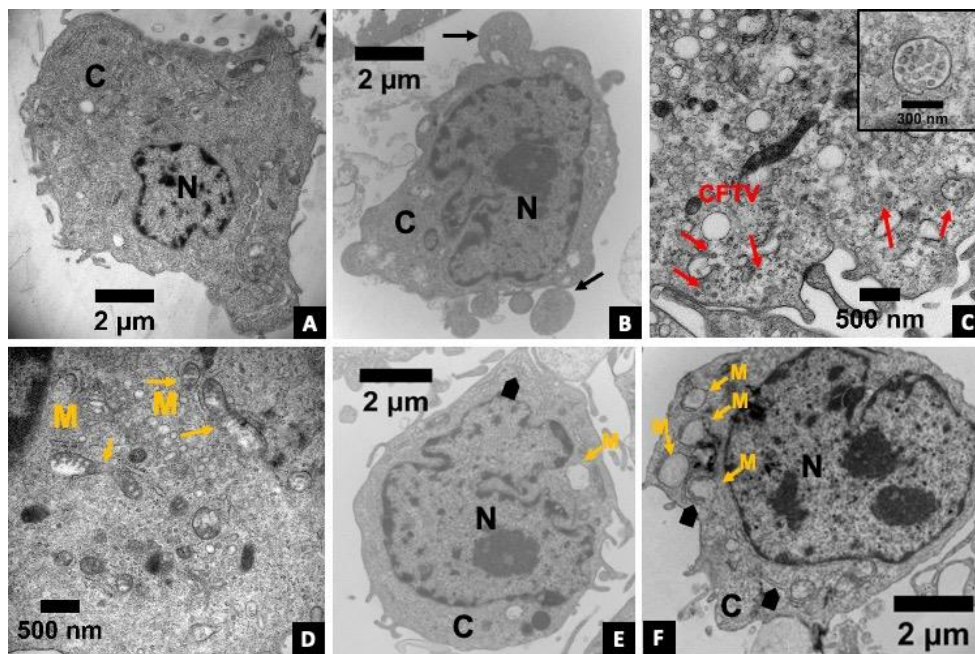


Figure 2. TEM images of CTFV-induced ultrastructural changes in HMEC-1 cells (A) uninfected HMEC-1 cell (B) infected HMEC-1 cell 24 hours post-infection at MOI 1.0 showing large bulbous projections. (C) presence of viral particles in the cytoplasm of infected cells (red arrows) as well as in vacuoles (insert shows high magnification). (D) Swollen mitochondria and mitochondrial membrane breakage (labeled as M) with loss of density in the matrix and cristae alterations (E and F) and dilated endoplasmic reticulum (black arrowheads). CTFV infected HMEC-1 cells show no presence of intra-nuclear and cytoplasmic fibrils (Figure 2B-F).

Discussion

Early studies have examined cells infected with CTFV using TEM; most of which focused on animal and insect cell lines (Oshiro and Emmons, 1968; Yunker and Cory, 1969). Previous reports on CTFV ultrastructure have shown cytoplasmic and nuclear fibrils, while the ultrastructural pathology induced by CTFV in human cells remains incompletely described. Notably, Philipp et al. (1993) reported ultrastructural changes in the human hematopoietic progenitor cell line KG-1a, the erythroblast cell line HEL, and primary human bone marrow CD34+ cells (Philipp et al., 1993).

In human progenitor cells, viral particles are often clustered around granular matrices and scattered throughout the cytoplasm (Philipp et al., 1993). HEL cells also showed arrays of filaments with interspersed viral particles on the cell's periphery with occasional intranuclear fibers (Philipp et al., 1993). Interestingly, this same study described cells infected for extended timepoints, up to 96 hours post-infection but did not describe cytopathic effects. In our studies using the Florio strain of CTFV, we see extensive apoptosis past 24 hours of infection with MOI of 1.0. The study by Philipp et al. (1993) used the R1517 strain of CTFV at an MOI of 1.0, a human isolate from Colorado that may have differences in virulence, allowing extended infection time points. The difference in CTFV pathogenesis may also be influenced by the cell types infected. It is likely that extensive apoptosis occurs in HMEC-1 at early time points and facilitates viral dissemination.

Our study observed that Vero and HMEC-1 cells infected with CTFV displayed increased vacuolization and mitochondrial breakdown at 24 hours post-infection compared to uninfected cells (Figures 1 and 2, respectively). Both infected cell types showed similar characteristics consisting of numerous vacuoles, bulbous surface projections, and mitochondria disruptions including swollen mitochondria and dissolved mitochondrial matrix in (Figure 1B, 2B and 2D-F). Vacuoles within infected Vero cells often appeared to be filled with cell contents, while the vacuoles within infected HMEC-1 cells contained virion particles, lamellar structures, or appeared empty (Figure 2 C).

Many cytosolic RNA viruses produce viral inclusion bodies, called viral factories or viroplasms, within the cytoplasm of infected cells that serve as a site for viral genome replication and assembly of progeny virions (Stanifer et al., 2017). Many viruses in the Reoviridae family induce two types of structurally distinct viroplasms, globular and filamentous. It is suggested that the globular factories are sites of RNA replication, and the filamentous factories are sites of virus assembly (Xie et al., 2017 and Attoui et al., 2012).

We, and others, have shown that CTFV infection results in the production of granular matrices in the cytoplasm of infected cells (Figure 1B insert) (Murphy et al., 1968; Oshiro and Emmons, 1968; Philipp et al., 1993). In this

study, these granular matrices are present in both cell lines, and additional fibrillar structures are present in Vero cells which are absent in CTFV-infected HMEC-1 cells at 24 hours post-infection. The granular matrices observed in the cytoplasm of CTFV-infected cells appear structurally similar to viral inclusion bodies produced during Orbivirus infections (Attoui et al., 2005). As seen in both infections, virus dense patches begin to develop within the cytoplasm. It is unclear how CTFV produces these granular matrices, but many viruses can utilize cellular filaments as a structural component for viral replication processes, which often produce a granular or filamentous-like structure at the site of replication (Parvate et al., 2020). For example, mammalian reovirus strain T3D inclusions contain microtubules and an intermediate filament, vimentin, that are rearranged to develop and surround the viral inclusions (Finstad et al., 2014).

Additionally, we observed fibrillar structures as single strands in the nucleus region of Vero cells and as grouped strands in the cytoplasm (Figure 1D). The role and etiology of these fibrillar structures in CTFV infection are currently unknown; however, studies involving similar fibrillar structures produced in other virus infections suggests that these structures may be associated with viral release, viral propagation to neighboring cells, or even viral packaging (Chen et al., 2019; Shah et al., 2017; Xie et al., 2017).

Furthermore, CTFV may utilize cellular filaments as structural support for virus replication. The fibers are antigenically related to CTFV, though it is unknown if they are composed of viral proteins or coated in viral protein (Oshiro and Emmons, 1968). The importance of the filamentous factories is highlighted in a recent study that showed that the T3D strain of reovirus produced globular virus factories had more empty virus particles after replication than a strain of reovirus that produced filamentous virus factories (T1L). This study suggests that viruses with filamentous virus factories are more efficient in genome packaging than those with globular virus factories (Shah et al., 2017). The virus factories produced by the T1L strain are associated with microtubules, and these microtubules appear as thicker filaments due to the accumulation of viral proteins around the microtubules (Shah et al., 2017). The granular matrices and fibrillar structures observed in the cytoplasm of CTFV-infected cells may be globular and filamentous viral factories where CTFV genome replication and virion assembly occur, respectively. However, further research is needed to determine these structures' function and determine if the filaments observed in CTFV-infected Vero cells increase CTFV replication and assembly.

Similar studies have reported that fibrillar structures aid in virus release and movement within the cells. Rice gall dwarf virus (RGDV), a plant reovirus, produces fibrillar structures in infected insect cells made up of a nonstructural virus protein, which targets the mitochondria's outer membrane and induces mitochondrial degeneration and subsequent apoptosis (Chen et al., 2019). Many CTFV-

infected Vero and HMEC-1 cells in our study display characteristics of apoptosis, such as more bulbous surface projections, increased vacuolization, and mitochondrial breakdown including swollen mitochondria and dissolved mitochondrial matrix (Figure 1B, 2B, and 2D-F). The role of the fibrillar structures observed in our study may be related to the cell apoptosis in Vero cells, and its selective presence in certain cell lines (present in Vero but not in HMEC-1 cells) requires further investigation. A more detailed and extensive examination is needed to determine these fibers' role on the mechanisms of CTFV induced cell death and its significance in viral pathology.

In addition to its role in viral replication and spread, as previously reported (Chen et al., 2019; Shah et al., 2017; Xie et al., 2017), the fibrillar structures observed in Vero cells could be the product of the cell's antiviral response to CTFV infection. Filament structures reported in other viral diseases, such as influenza and vesicular stomatitis virus, were shown to develop similar structures due to cell antiviral response (Sehgal et al., 2020; Verhelst et al., 2013). In these studies, type I and III interferons produced by infected cells increased Mx production, a protein that inhibits viral replication. The subsequent build-up of Mx protein complexes forms cytoplasmic and nuclear filament-like structures (Sehgal et al., 2020; Verhelst et al., 2013). Further studies on the production or absence of these fibers during CTFV infection may provide insight into CTFV pathogenic mechanisms among specific cell types or virus strains.

Our study has shown that CTFV induces specific ultrastructural changes in a cell type-dependent manner. Our present findings will enable further investigation into the presence, composition, and function of these viral-induced fibers in select cell types. Furthermore, studies aimed at examining the endomembrane system and the potential reorganization of cellular membrane compartments would enhance our understanding of viral replication and pathology. Understanding these fibrillar structures and morphological changes due to CTFV infections will extend our knowledge towards CTFV pathogenesis and viral replication.

Acknowledgments

CTFV was provided by the World Reference Center for Emerging Viruses and Arboviruses through the University of Texas Medical Branch at Galveston.

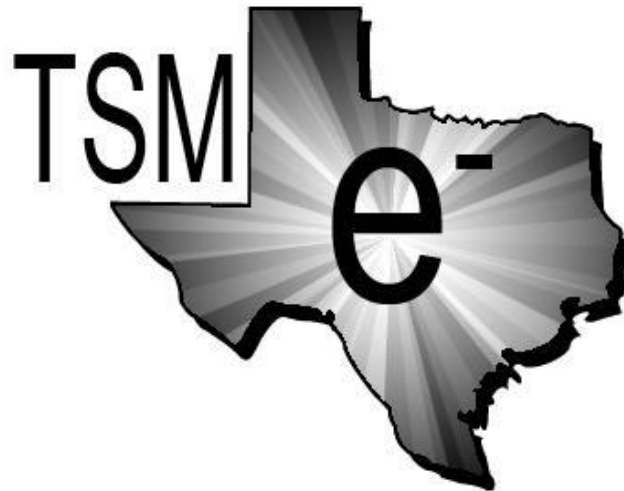
Funding

This work was supported from the SHSU New Faculty Grant Program.

References

- Attoui, H., Jaafar, F.M., De Micco, P., De Lamballerie, X., 2005. Coltiviruses and Seadornaviruses in North America, Europe, and Asia. *Emerg. Infect. Dis.* <https://doi.org/10.3201/eid1111.050868>
- Chen, Q., Zheng, L., Mao, Q., Liu, J., Wang, H., Jia, D., Chen, H., Wu, W., Wei, T., 2019. Fibrillar structures induced by a plant reovirus target mitochondria to activate typical apoptotic response and promote viral infection in insect vectors. *PLoS Pathog.* <https://doi.org/10.1371/journal.ppat.1007510>
- Emmons, R.W., 1988. Ecology of Colorado tick fever. *Annu. Rev. Microbiol.* <https://doi.org/10.1146/annurev.mi.42.100188.000405>
- Finstad, Ø.W., Dahle, M.K., Lindholm, T.H., Nyman, I.B., Løvoll, M., Wallace, C., Olsen, C.M., Storset, A.K., Rimstad, E., 2014. Piscine orthoreovirus (PRV) infects Atlantic salmon erythrocytes. *Vet. Res.* <https://doi.org/10.1186/1297-9716-45-35>
- Goldsmith, C.S., Miller, S.E., 2009. Modern uses of electron microscopy for detection of viruses. *Clin. Microbiol. Rev.* <https://doi.org/10.1128/CMR.00027-09>
- Goodpasture, H.C., Poland, J.D., Francy, D.B., Bowen, G.S., Horn, K.A., 1978. Colorado tick fever: clinical, epidemiologic, and laboratory aspects of 228 cases in Colorado in 1973-1974. *Ann. Intern. Med.* <https://doi.org/10.7326/0003-4819-88-3-303>
- Karatsos, N., Poland, J.D., Emmons, R.W., Mathews, J.H., Calisher, C.H., Wolff, K.L., 1987. Antigenic variants of Colorado tick fever virus. *J. Gen. Virol.* <https://doi.org/10.1099/0022-1317-68-5-1463>
- Krauss, H., Weber, A., Appel, M., Enders, B., Isenberg, H.D., Schiefer, H.G., Slenczka, W., von Graevenitz, A., Zahner, H., Bakken, J.S., 2004. Zoonoses: Infectious Diseases Transmissible from Animals to Humans, 3rd Edition: Zoonoses: Infectious Diseases Transmissible from Animals to Humans, 3rd Edition. *Clin. Infect. Dis.* <https://doi.org/10.1086/383066>
- Murphy, F.A., Coleman, P.H., Harrison, A.K., Gary, G.W., 1968. Colorado tick fever virus: An electron microscopic study. *Virology.* [https://doi.org/10.1016/0042-6822\(68\)90302-4](https://doi.org/10.1016/0042-6822(68)90302-4)
- Oshiro, L.S., Dondero, D. V., Emmons, R.W., Lennette, E.H., 1978. The development of Colorado tick fever virus within cells of the haemopoietic system. *J. Gen. Virol.* <https://doi.org/10.1099/0022-1317-39-1-73>
- Oshiro, L.S., Emmons, R.W., 1968. Electron microscopic observations of Colorado tick fever virus in BHK 21 and KB cells. *J. Gen. Virol.* <https://doi.org/10.1099/0022-1317-3-2-279>
- Parvate, A., Sengupta, R., Williams, E.P., Xue, Y., Chu, Y.K., Stahelin, R. V., Jonsson, C.B., 2020. Cryofixation of Inactivated Hantavirus-Infected Cells as a Method for Obtaining High-Quality Ultrastructural Preservation for Electron Microscopic Studies. *Front. Cell. Infect. Microbiol.* <https://doi.org/10.3389/fcimb.2020.580339>
- Philipp, C.S., Callaway, C., Chu, M.C., Huang, G.H., Monath, T.P., Trent, D., Evatt, B.L., 1993. Replication of Colorado tick fever virus within human hematopoietic progenitor cells. *J. Virol.* <https://doi.org/10.1128/jvi.67.4.2389-2395.1993>
- Roingard, P., Raynal, P.I., Eymieux, S., Blanchard, E., 2019. Virus detection by transmission electron microscopy: Still useful for diagnosis and a plus for biosafety. *Rev. Med. Virol.* <https://doi.org/10.1002/rmv.2019>

- Schneider, C.A., Rasband, W.S., Eliceiri, K.W., 2012. NIH Image to ImageJ: 25 years of image analysis. *Nat. Methods*. <https://doi.org/10.1038/nmeth.2089>
- Schrand, A.M., Schlager, J.J., Dai, L., Hussain, S.M., 2010. Preparation of cells for assessing ultrastructural localization of nanoparticles with transmission electron microscopy. *Nat. Protoc.* <https://doi.org/10.1038/nprot.2010.2>
- Sehgal, P.B., Yuan, H., Scott, M.F., Deng, Y., Liang, F.X., Mackiewicz, A., 2020. Murine GFP-mx1 forms nuclear condensates and associates with cytoplasmic intermediate filaments: Novel antiviral activity against VSV. *J. Biol. Chem.* <https://doi.org/10.1074/jbc.RA120.015661>
- Shah, P.N.M., Stanifer, M.L., Höhn, K., Engel, U., Haselmann, U., Bartenschlager, R., Kräusslich, H.G., Krijnse-Locker, J., Boulant, S., 2017. Genome packaging of reovirus is mediated by the scaffolding property of the microtubule network. *Cell. Microbiol.* <https://doi.org/10.1111/cmi.12765>
- Spurr, A.R., 1969. A low-viscosity epoxy resin embedding medium for electron microscopy. *J. Ultrastructure Res.* [https://doi.org/10.1016/S0022-5320\(69\)90033-1](https://doi.org/10.1016/S0022-5320(69)90033-1)
- Stanifer, M.L., Kischnick, C., Rippert, A., Albrecht, D., Boulant, S., 2017. Reovirus inhibits interferon production by sequestering IRF3 into viral factories. *Sci. Rep.* <https://doi.org/10.1038/s41598-017-11469-6>
- Verhelst, J., Hulpiau, P., Saelens, X., 2013. Mx Proteins: Antiviral Gatekeepers That Restrain the Uninvited. *Microbiol. Mol. Biol. Rev.* <https://doi.org/10.1128/mubr.00024-13>
- Xie, L., Lv, M., Fang, Song, X.J., Yang, J., Li, J., Sun, Z.T., Zhang, Y.Y., Chen, J.P., Zhang, H.M., 2017. Structure and components of the globular and filamentous viroplasms induced by Rice black-streaked dwarf virus. *Micron.* <https://doi.org/10.1016/j.micron.2017.03.002>
- Yunker, C.E., Cory, J., 1969. Colorado Tick Fever Virus: Growth in a Mosquito Cell Line. *J. Virol.* <https://doi.org/10.1128/jvi.3.6.631-632.1969>



A RAPID METHOD TO CHARACTERIZE CELLULOSE FIBRILS USING SCANNING ELECTRON MICROSCOPY

MARINA R. MULENOS¹, BERND ZECHMANN²,
AND CHRISTIE M. SAYES^{1*}

¹ Department of Environmental Science, Baylor University, Waco, Texas, USA

² Center for Microscopy and Imaging, Baylor University, Waco, Texas, USA

*Corresponding author (Christie_Sayes@baylor.edu)

Abstract

Cellulose is a renewable resource used in consumer products including paper and mill, food packaging, and cosmetics. Over the years, there has been an increase in the use of mechanically processed cellulose structures into more advantageous nanocrystalline and fibrillated forms. Morphological characterization of these cellulosic forms is necessary to understand the properties related to bioavailability and eventual fate in the environment. Organic nanomaterials are difficult to characterize microscopically. Artifacts induced by agglomeration are common. Here, we describe a rapid and inexpensive method to prepare cellulose fibrils in the post-production phase via scanning electron microscopy. The cellulose was set overnight in LR White embedding medium. Then, the cellulose was sputter coated with a 5 nm layer of iridium to decrease sample charging. Compared to previous preparation methods of aqueous suspensions of cellulose, this embedding method reduced the aggregation of fibrils. With this method it was possible to elucidate important structural conformations of the cellulose fibrils. This method not only produced images with distinguishable fibers, but also allowed for the understanding of fibril networks. The preparation method can be used to identify key structural characteristics of fibrillated substances to aid in new product development while ensuring occupational health.

Keywords: sample preparation; scanning electron microscopy; cellulose; sample preservation

Introduction

Cellulose is a renewable resource used in consumer and industrial processes through the modification of wood pulp. Due to the expansive use of cellulose over a wide range of multidisciplinary applications, there is a measurable inhalation, dermal, and ingestion exposure to both occupational workers and consumers (Howard and Murashov, 2009; Kargarzadeh et al., 2018; Shatkin and Kim, 2015). Health and safety research has recognized the importance of completing a comprehensive physicochemical characterization of newly synthesized and engineered materials for many years (Fadeel et al., 2015). Engineered forms of cellulose ought to be fully characterized for both structural and chemical properties to aid in new product development while ensuring occupational health (Zielińska et al., 2020).

In industry and throughout the literature, transmission electron microscopy (TEM) is widely used for characterizing materials within the sub micrometer and nanometer scale. TEM is a powerful technique which produces two dimensional black and white images at Angstrom level resolution making it the preferred technique among material scientists (Foster et al., 2018; Sadik et al., 2014). However, there are challenges associated with using TEM for characterization including; aggregation, drying effects and/or inducing artifacts through the use of staining techniques (Michen et al., 2015). When characterizing materials, it is of utmost importance to understand the chemical and physical properties sans artifacts because false findings or incorrect assumptions in morphological characterization can have consequences regarding health and safety.

Recent reports address the different artifacts among various sample preparation methods. For example, characterization using scanning electron microscopy (SEM) of lyophilized cellulose fibers using sputter coating before imaging has been shown (Eyholzer et al., 2010). One setback with this method is that lyophilization may induce increasing drying effects and may not produce data indicative of the material in the use-phase. Other studies have reported a technique which sprinkles dried cellulose on carbon adhesive tape or on glass plates (Eyholzer et al., 2010; Ho et al., 2011; Perić et al., 2019; Xhanari et al., 2011). The methods previously mentioned require high vacuum in the SEM and may pose certain risks to contaminating the column and altering the vacuum of the SEM or may show drying effects depending on the water percentage of the sample. Consequently, most physicochemical characterization of cellulose lack a 'one size fits all' method for proper sample preparation conditions (Foster et al., 2018; Ogawa and Putaux, 2019).

In this paper, we report for the first time, a sample preparation method commonly used for the TEM into a rapid method for imaging cellulose with the SEM. This method can be used to identify key structural characteristics of materials to aid in the product development process. The method establishes an easy way to visualize critical characteristics of materials without producing artifacts.

Materials and Methods

Light microscopy: Sample preparation and imaging.

Cellulosic materials were suspended in ultrapure water

(18.2 mΩ) at a 1:1000 dilution and allowed to dry at room temperature (25°C) on a glass microscope slide. Light microscopy was completed using an Olympus Corporation (Tokyo, Japan) Stereomicroscope SZX16. Images were taken in the oblique mode to increase contrast.

Scanning electron microscopy sample preparation. In triplicate, cellulosic materials were suspended in ultrapure water (18.2 mΩ) at a 1:1000 dilution and allowed to dry at room temperature on carbon adhesive tape (EMS, Hatfield, PA, US). Once dried, samples were sputter coated (ACE 600 Sputter coater, Leica Microsystems, Wetzlar, Germany) with a 5 nm thick layer of iridium.

For sample preparation of the dry powder form, cellulose was weighed out on an analytical balance (Mettler Toledo, Columbus, OH, US) and placed in an aluminum dish. To prepare the resin, LR White embedding medium (Electron microscopy sciences, EMS, Hatfield, PA, US) was placed in a plastic cup and 2 drops of the accelerator were added and mixed thoroughly. Ten (10) mL of LR White was poured into the aluminum dish and mixed with the cellulose powder.

Sample trimming and sputter coating. Preserved samples in the polymerized medium were trimmed using an EM Trim 2 (Leica, Wetzlar, Germany) trimmer with 20,000 rpm and a 1 μm step. Samples were trimmed to expose cured cellulose fibrils. Once trimmed, samples were sputter coated with an ACE600 sputter coater with a 10 nm iridium layer thickness. Sputter coating was used to decrease sample charging.

Image acquisition and processing. SEM imaging was acquired with a Versa 3D SEM (FEI Company, Hillsboro, OR, US) using the ICE detector, at 5 kV, with a 3.0 mm working distance, in high vacuum mode. At least ten images were acquired for each sample. Post image processing was conducted with ImageJ (National Institutes of Health) and data visualization was completed in Microsoft Power Point.

Results

Wood pulp is processed into cellulose bulk material (often referred to as conventional cellulose) and when further processed, cellulose fibrils and nanocrystals can be isolated (Figure 1). Conventional cellulose aggregates exist in various lengths and widths in the micrometer size range. Fibrils contain a vast network of individual intermingling structures.

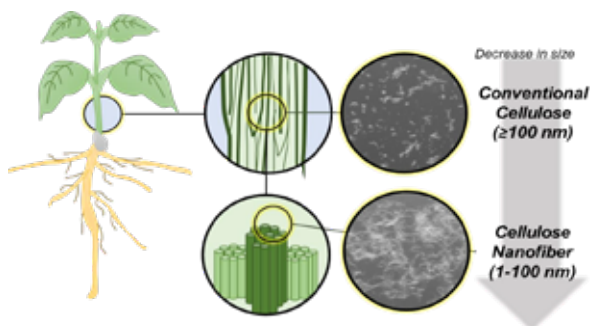


Figure 1. Cellulose is a multi-functional renewable, organic, and sustainable material. Fibrillated cellulose is routinely

used in consumables, food packaging, and cosmetics. Due to the vast number of products that cellulose and cellulosic derivatives are incorporated into, there is a high potential for exposure. It is important to characterize modified cellulose created from wood pulp to inform health and safety guidelines. Electron microscopy is the standard for characterizing these organic materials.

Cellulose samples were imaged using SEM. Fibrils were first prepared by suspending the sample with ultra-pure water and drying on to carbon adhesive tape. (Figure 2A, 2B) This sample preparation method displays an overlapping, aggregated, network of fibrous “sheets”. Individual fibers cannot be distinguished between each other due to aggregation. Additionally, there is low contrast between the background and the sample. Cellulose fiber powders utilizing LR White were imaged using SEM (Figure 2C, 2D). The sample preparation method produced images of distinct fibers with a high contrast from the background. Large and small fibers can be clearly differentiated, and the structure can be well characterized due to the absence of induced aggregation from sample preparation methods. Fibril width is resolved and enables quantitative width measurements.

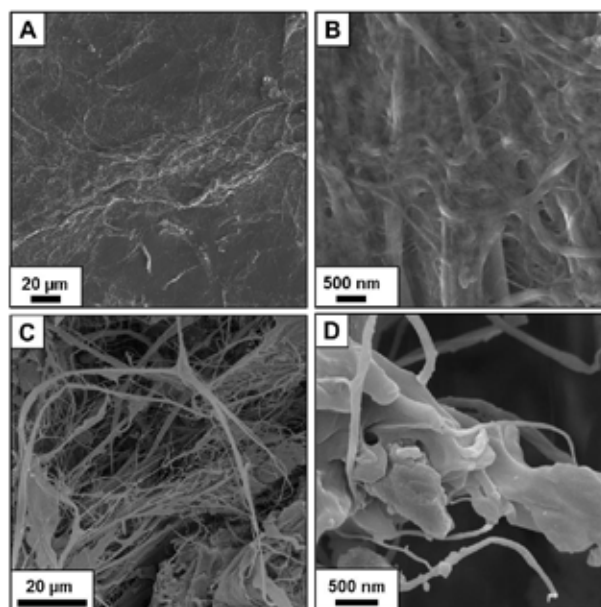


Figure 2. Comparison of Cellulose Sample Preparation Methods. Cellulosic fibrils were prepared by drying the cellulose suspension on carbon adhesive tape (A) and (B). The sample morphology shows sheets of cellulose with few fibers. Panels (C) and (D) were prepared by embedding dry powder materials in LR White. Panels (A) and (C) have a 20 μm scale bar, and panels (B) and (D) have 500nm scale bars for sample method comparison. Fibers are well resolved and easily identifiable. Images taken on a SEM, 5kV, ICE detector, spot size 5.0, working distance 3.0 mm, in high vacuum mode.

Discussion

Using LR White medium for sample preparation has been established for many years (Newman et al., 1982, Skepper and Powell, 2008). LR White is an acrylic resin with relatively low toxicity, low viscosity (8 cps), and high beam stability in the electron microscope. Thus, it is well suited for delicate biological samples such as cells, animal, and plant tissues as it infiltrates the sample rapidly, does not induce many artifacts or disturb the sample, and preserves the antigenicity. The application of LR White for the preparation of cellulose fibers demonstrated in this study displays a cost-effective, rapid, and repeatable method for the characterization of cellulose materials via SEM without producing artifacts or structural deformations. Compared to traditional methods used to image cellulose fibers, such as negative-stain imaging via TEM or deposit of aqueous solution onto adhesive tape imaged via SEM (Foster et al., 2018), the method described here resulted in a noticeable decrease in artificial aggregation, increase in contrast, and an increase in resolution. Not only is this method effective at characterizing morphology but is rapid and accessible to most laboratories.

Conclusion

We described a new sample preparation method for SEM that does not introduce chemical or physical alterations to the material being analyzed. The method proved that preservation of cellulosic structures can be done, which is important for the collection of accurate data, allowing a more comprehensive morphological understanding for physicochemical data analysis.

Funding

This work was partially funded by a grant from the P3Nano public-private partnership between the United States Endowment for Forestry and Communities and the U.S. Department of Agriculture, U.S. Forest Service Forest Products Laboratory in collaboration with Vireo Advisors, LLC.

References

- Eyholzer, C., Bordeanu, N., Lopez-Suevos, F., Rentsch, D., Zimmermann, T., & Oksman, K. (2010). Preparation and characterization of water-redispersible nanofibrillated cellulose in powder form. *Cellulose*, 17(1), 19-30.
- Fadeel, B., Fornara, A., Toprak, M. S., & Bhattacharya, K. (2015). Keeping it real: The importance of material characterization in nanotoxicology. *Biochemical and biophysical research communications*, 468(3), 498-503.
- Foster, E. J., Moon, R. J., Agarwal, U. P., Bortner, M. J., Bras, J., Camarero-Espinosa, S., . . . Eichhorn, S. J. (2018). Current characterization methods for cellulose nanomaterials. *Chemical Society Reviews*, 47(8), 2609-2679.
- Ho, T., Zimmermann, T., Hauert, R., & Caseri, W. (2011). Preparation and characterization of cationic nanofibrillated cellulose from etherification and high-shear disintegration processes. *Cellulose*, 18(6), 1391-1406.
- Howard, J., & Murashov, V. (2009). National nanotechnology partnership to protect workers. *Journal of Nanoparticle Research*, 11(7), 1673-1683.
- Kargarzadeh, H., Mariano, M., Gopakumar, D., Ahmad, I., Thomas, S., Dufresne, A., . . . Lin, N. (2018). Advances in cellulose nanomaterials. *Cellulose*, 25(4), 2151-2189.
- Michen, B., Geers, C., Vanhecke, D., Endes, C., Rothen-Rutishauser, B., Balog, S., & Petri-Fink, A. (2015). Avoiding drying-artifacts in transmission electron microscopy: Characterizing the size and colloidal state of nanoparticles. *Scientific reports*, 5, 9793.
- Newman, G., Jasani, B., & Williams, E. (1982). The preservation of ultrastructure and antigenicity. *Journal of Microscopy*, 127(3), RP5-RP6.
- Newman, G., Jasani, B., & Williams, E. (1983). A simple post-embedding system for the rapid demonstration of tissue antigens under the electron microscope. *The Histochemical journal*, 15(6), 543-555.
- Ogawa, Y., & Putaux, J.-L. (2019). Transmission electron microscopy of cellulose. Part 2: technical and practical aspects. *Cellulose*, 26(1), 17-34.
- Perić, M., Putz, R., & Paulik, C. (2019). Influence of nanofibrillated cellulose on the mechanical and thermal properties of poly (lactic acid). *European Polymer Journal*, 114, 426-433.
- Sadik, O., Du, N., Kariuki, V., Okello, V., & Bushlyar, V. (2014). Current and emerging technologies for the characterization of nanomaterials. *ACS Sustainable Chemistry & Engineering*, 2(7), 1707-1716.
- Shatkin, J. A., & Kim, B. (2015). Cellulose nanomaterials: life cycle risk assessment, and environmental health and safety roadmap. *Environmental Science: Nano*, 2(5), 477-499.
- Skepper, J. N., & Powell, J. M. (2008). Immunogold staining of London Resin (LR) White sections for transmission electron microscopy (TEM). *Cold Spring Harbor Protocols*, 2008(6), pdb. prot5016.
- Xhanari, K., Syverud, K., Chinga-Carrasco, G., Paso, K., & Stenius, P. (2011). Structure of nanofibrillated cellulose layers at the o/w interface. *Journal of colloid and interface science*, 356(1), 58-62.
- Zielińska, A., Costa, B., Ferreira, M. V., Miguéis, D., Louros, J., Durazzo, A., . . . Morsink, M. (2020). Nanotoxicology and nanosafety: Safety-by-design and testing at a glance. *International Journal of Environmental Research and Public Health*, 17(13), 4657.

MORPHOLOGICAL STUDY OF THE OVIPOSITOR OF THREE SPECIES OF *PLEIDAE* (INSECTA: HEMIPTERA) USING THE SCANNING ELECTRON MICROSCOPE

JERRY L. COOK* AND RAJESH BALARAMAN

Department of Biological Sciences, Sam Houston State University, Huntsville, TX 77341-2116

¹*Corresponding author (jcook@shsu.edu)

Abstract

This study documents the morphology and sensilla of three species of *Pleidae*, *Paraplea brunni*, *P. frontalis*, and *Neoplea borellii*. The first gonapophysis of the ovipositor in these three species of *Pleidae* exhibit similar structures but different arrangements and numbers of these structures differ and appear to be species specific. The first gonapophysis of all species has teeth along the posterior margin and the posterior part of the ventral margin. Some of these teeth appear immovable and some appear to be moveable due to arising from a socket. Basiconica sensilla are found anterior to the posterior margin in all species surveyed. These likely have a mechanosensory role in oviposition but could be chemosensory. Long trichoid sensilla are located on the ventral surface of the first gonapophysis of all species and some species also have short trichoid sensilla anterior to the basiconica sensilla.

Keywords: functional anatomy, sensilla, gonapophysis, *Neoplea*, *Paraplea*

Introduction

Species in the family *Pleidae* are small aquatic insects most commonly found in vegetated areas of quiet waters. In this habitat, they swim in an inverted position, earning them the common name of pygmy backswimmers. They feed mostly on small arthropods and are thought to deposit their eggs in plant tissue (Schuh and Weirauch 2020). Wefelscheid (1912) was first to give a description of the pleid ovipositor in his study of *Plea minutissima* Leach, and he documented the functional morphology of this structure to allow eggs to be deposited into plant tissue.

The ovipositor is not only important biologically as a means of depositing eggs (Emeljanov 2014), but is also of taxonomic importance in identifying species (Pendegrast 1957, Scudder 1959, Cook 2011) and understanding phylogenies (Zhong et al. 2017). Specifically, the first gonapophysis of species in *Pleidae* and its sister taxon *Helotrephidae* appears to be taxonomically important due to the consistency in its structure of morphological characters within a species (Papáček 2002, 2008; Cook 2011). The first gonapophysis is only part of the pleid ovipositor but it contains most of the functional morphology.

The morphology of the insect ovipositor has evolved to facilitate the deposition of eggs in a favorable location to increase the success for that species, and structures of the ovipositor likewise suggest its function. In the invasive fruit fly, *Drosophila suzukii* (Matsumura), the ovipositor is modified to deposit eggs in ripening fruit instead of the soft rotting fruit used by most species of *Drosophila*. The modifications of the ovipositor in *D. suzukii* include an enlarged serrated ovipositor with multiple contact sensory structures (Crava et al. 2020). This same general adaptation is also seen in members of the family *Pleidae*. An important innovation of an ovipositor to deposit within a stiff substrate is the development of cutting tooth-like structures but there are also mechanosensitive sensilla to

facilitate the deposition of eggs (Karkali and Martin-Blanco 2017, Atallah et al. 2014). Different ultrastructural elements of the ovipositor have evolved to correspond with preferred ovipositional substrates (Craddock et al. 2018).

Only a few studies have addressed the morphology of the ovipositor in *Pleidae*, and all of these studies made observations at low magnifications. The first gonapophysis of *Pleidae* was illustrated by Lundblad (1933), Bachman (1968), Roback and Nieser (1974), Nieser (1975), Benzie (1989), Sublett and Cook (2015) and Cook et al. (2020). All of these studies presented general shape of the first gonapophysis, arrangement of teeth, and presence of hairs. However, these structures were not studied at a magnification that could detect ultrastructure or the presence of additional characteristics of this structure. The knowledge of this ultrastructure likewise allows insight into the function of these structures. The study herein is the first to document the microanatomy of the first gonapophysis of the ovipositor in *Pleidae* by means of scanning electron microscopy (SEM), and we show differences between three species from two genera of *Pleidae*.

Materials and methods

Specimens used for this study were from museum collections housed in the Sam Houston State University Natural History collections. All specimens were originally pinned but were taken off of pins prior to mounting for SEM observations. The ovipositor of each specimen was naturally exposed in the specimen and no additional manipulation was made before observation. We observed at least three specimens of each species to ensure that there was no morphological variation in the number and placement of structures on the ovipositor of these species. Our finding of similarity within the species coincided with the findings of Sublett and Cook (2015). Specimen data for species included in the study is as follows:

Paraplea brunni (Kirkaldy), det.: J. L. Cook, Australia, Northern Territory, Howard River at Gunnpoint Road, 12 September 2002, G. Chalet

Paraplea frontalis (Fieber), det.: J. L. Cook, Thailand, Northeastern Thailand, 15 January 1953, M. E. Griffith

Neoplea borellii (Kirkaldy), det.: J. L. Cook, Brazil, Nova Teutonia, 27°11'S, 52°23'W, Fritz Plauman

Specimens for SEM imaging were prepared by mounting the biological specimens onto the SEM stub using carbon tape. Mounting of samples on the carbon stub was done under a stereo microscope. The specimen was sputter coated with gold for 90 sec (300A) using a Cressington 108 sputtercoater, Cressington Scientific Instruments, 34 Chalk Hill, Watford, England. The gold sputtered specimen were imaged under high vacuum with acceleration voltage ranging from 1-10kV and a working distance of 5 mm. The images were captured using a Hitachi SU3500 SEM with secondary electron detector. The specimen stage was tilted (max 5 degrees) whenever required. The charging of the specimen was prevented by reducing the kV and spot size respectively (Murtey and Ramasamay, 2015). The image of the wholmount of *Paraplea frontalis* was taken using a Keyence VHX-6000 microscope.

Results

The first gonapophysis of the ovipositor of *P. brunni* (Fig. 1A) includes an apical row of four upper immovable teeth and two lower teeth that appear slightly flexible. The

movable teeth are in a socket but are oriented posteriorly as are the immovable teeth, which are fused to the cuticle of the gonapophysis and not in a socket. These apical teeth are on the margin of the gonapophysis. There are also three movable teeth along the ventral surface of the gonapophysis, each equally distanced from each other (~11µm apart at the base) and situated toward the apical part of the gonapophysis. These apical moveable (socketed) teeth do not appear to have as much range of movement as the internal teeth, tooth-like structures posterior to the apex and not on the margins are different in structure than the marginal teeth. These structures are cone shaped, coming to a blunt point at the apex and are attached into a socket by a narrower trunk (Fig. 1A, 1B). These pegs clearly fit the definition of basiconica sensilla, although their shape is different from reports of these structures in other insects. Each first gonapophysis of *P. brunni* (there is a right and left gonapophysis) has eight of these structures (Fig. 1A). The basiconica sensilla of *P. brunni* range in size from 5.8 to 13.5 µm and some are symmetrical and some curved (Fig. 1C). Posterior to the basiconica sensilla are two irregular rows of trichoid sensilla and arise from flexible sockets. These are short hair-like structures That are 8.4 µm or less. (Fig. 1A, 1D). Each gonapophysis has two long Trichoid sensilla emerging near the ventral edge of the first gonapophysis (Fig. 1A). These long trichoid sensilla are curved and about 120 µm long.

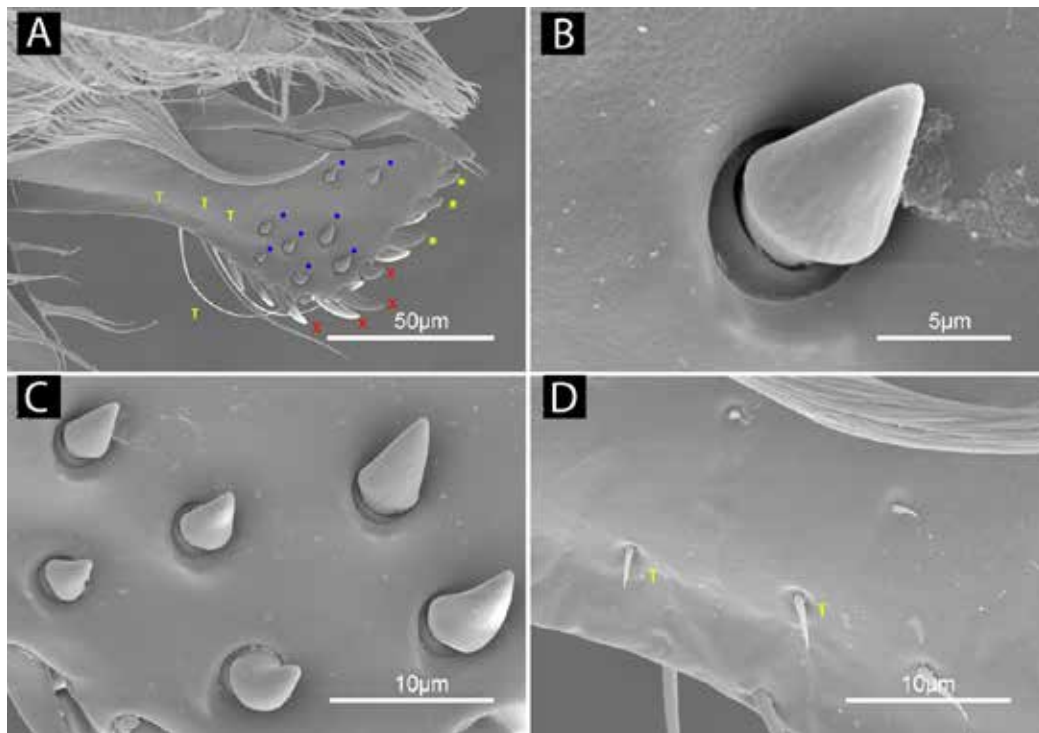


Figure 1. Ovipositor morphology of *Paraplea brunni*. (A) Ovipositor of *Paraplea brunni* showing toothed first gonapophysis. A yellow asterisk designates an immovable apical tooth, a red x designates a moveable tooth, a yellow T shows a trichoid sensilla, and a blue solid circle represents a basiconica sensilla. Scale bar = 50µm. (B) Basiconica sensilla of interior of first gonapophysis of *Paraplea brunni*. Scale bar = 5µm. (C) Basiconica sensilla on the first gonapophysis of *Paraplea brunni*. Scale bar = 10µm. (D) Trichoid sensilla, labelled with a yellow T, on the first gonapophysis of *Paraplea brunni*. Scale bar = 10µm.

The first gonapophysis of the ovipositor of *P. frontalis* is similar in structure to that of *P. brunni* but there are differences in shape and number of structures. The apical

margin has only two dorsal teeth that are fused and immovable and a dorsal apical ridge that appears serrated.

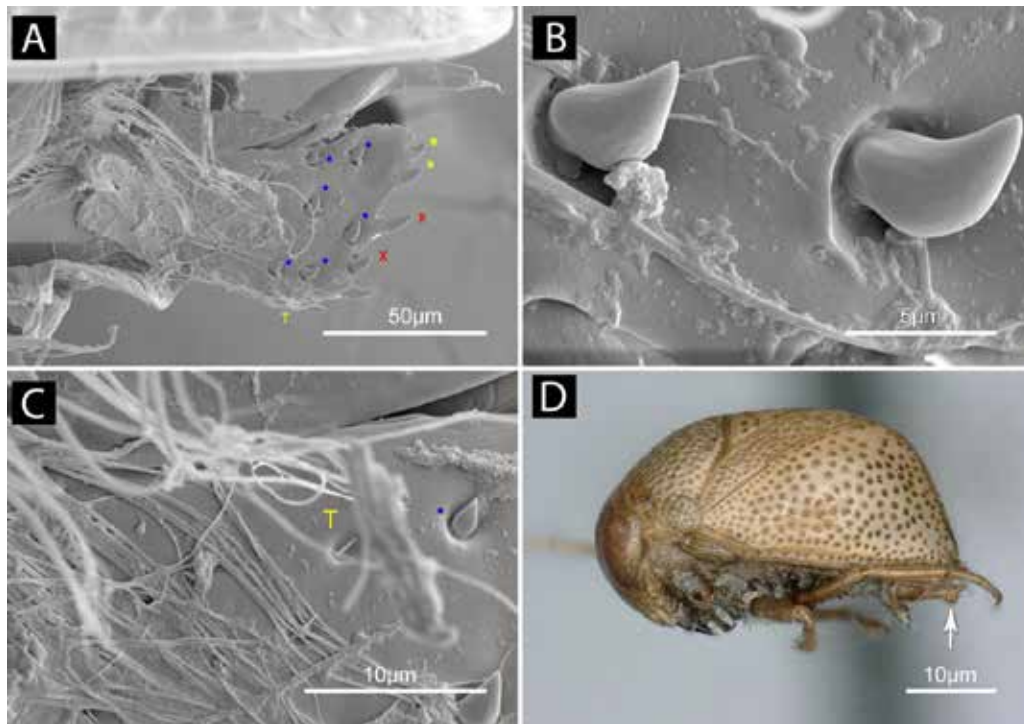


Figure 2. Ovipositor morphology of *Paraplea frontalis*. (A) Ovipositor of *Paraplea frontalis* showing gonapophysis. A yellow asterisk designates an immovable apical tooth, a red x designates a moveable tooth, a yellow T shows a trichoid sensilla, and a blue solid circle represents a basiconica sensilla. Scale bar = 50µm. (B) Basiconica sensilla of *Paraplea frontalis*. Scale bar = 50µm. Scale bar = 5µm. (C) Short trichoid sensilla, designated by a yellow T, to the right (anterior) to the basiconica sensilla, designated as a blue circle, of *P. frontalis*. Scale bar = 10µm. (D) Lateral view of *Paraplea frontalis* with arrow pointing to gonapophysis of the ovipositor. Scale bar = 0.5mm.

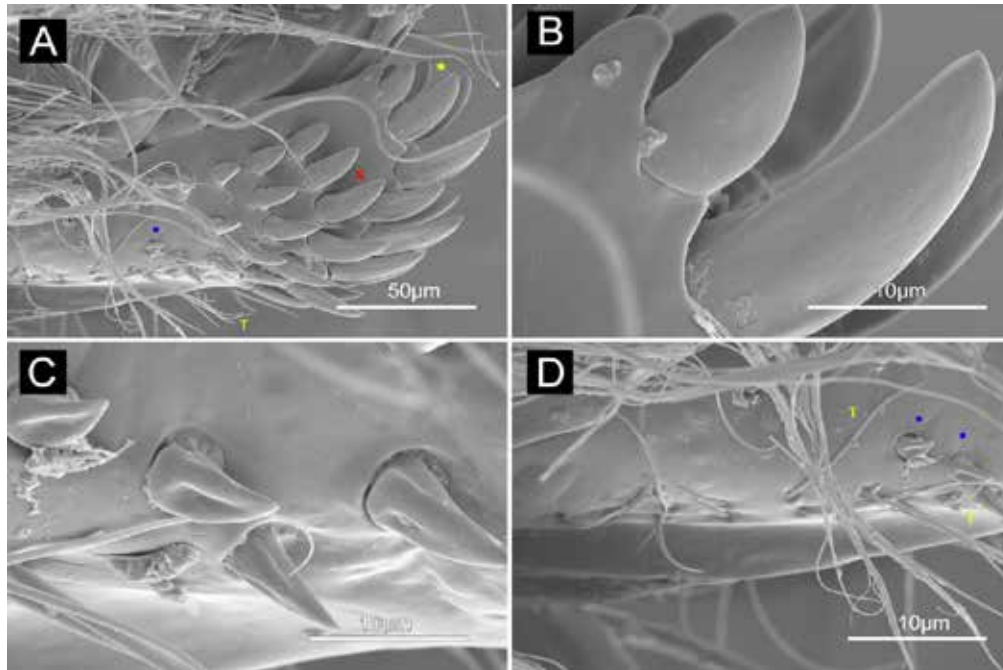
The three other apical teeth arise from sockets, although the socket does not appear to allow a great deal of movement (Fig. 2A) although the ventral two in this row appear to be basiconica sensilla (Fig. 2A, 2B). The ventral margin also has three moveable teeth (Fig. 2A). There are nine basiconica sensilla posterior to the apical margin, which are generally arranged in vertical rows (designated as primary and secondary teeth by Sublette and Cook (2015)). All basiconica sensilla of *P. frontalis* are curved and range in size from 7.7 to 16.0 µm. There are two short trichoid sensilla similar to the small trichoid sensilla of *P. brunni* but are shorter, measuring 4.9 µm. These are just anterior to the last basiconica sensilla (Fig. 2C). Each first gonapophysis has two long trichoid sensilla that resemble those of *P. brunni* but are slightly more anterior along the anterior margin. The location of the gonapophysis of the ovipositor is shown in Fig. 2D and is the same location in all *Pleidae*.

The first gonapophysis of *Neoplea borellii* is more heavily toothed than is seen in the genus *Paraplea*. Teeth in *N. borellii* are not only found on the apical and ventral margins, but these structures are also found throughout much of the anterior half of the first gonapophysis (Fig. 3A). The apical

margin of the gonapophysis, which would be directed posteriorly has teeth and sharp cuticular points. The cuticle at the upper margin has large serrations that resemble teeth. The topmost of these is blunt but the following four serrations come to a sharp point (Fig. 3A, 3B). The upper three teeth of the apex appear fused and immovable, but these are followed by three moveable teeth in a socket. The ventral margin has two moveable teeth that are shorter than those found on the apical margin, but these ventral teeth are oriented posteriorly in the manner of the marginal teeth. It is difficult to classify the first two vertical rows of structures anterior to the marginal teeth in *N. borellii*. These structures (termed primary and secondary teeth in the Sublette and Cook (2015) classification) resemble somewhat both the marginal apical teeth and basiconica sensilla, and these structures may have a dual function as mechanical cutting structures as well as a mechanosensory function. The largest of these are consistent in structure to apical (mechanical cutting) teeth while the smallest more resembles the basiconica sensilla as seen in the *Paraplea* species of this study (Fig. 2D). These structures of *N. borellii* transition in size, being largest near the ventral apex and smallest as the

first of a third row (tertiary tooth). Sizes on the non-margin teeth range from 20.0 to 58.2 μm . Posterior to the teeth are dorsal and ventral rows of basiconica sensilla, which are located near, but not on, the margins (Fig. 3A). This form of basiconica sensilla differs from those of *Paraplea* in that *N. borellii* has distinct ridges (Fig. 3C). Several trichoid sensilla

arise from flexible sockets along the ventral margin of the first gonapophysis in *N. borellii*. While there seem to always be two of these in *P. brunni*, there may be up to ten in *N. borellii*. All of the trichoid sensilla (Fig. 3D) appear to be about 75.0 μm . There were no short trichoid sensilla on the ovipositor of *Paraplea* as were found in *Neoplea*.



Figures 3. Ovipositor morphology of *Neoplea borellii*. (A) Ovipositor of *Neoplea borellii* showing heavily toothed gonapophysis. A yellow asterisk designates an immovable apical tooth, a red x designates a moveable tooth, a yellow T shows a trichoid sensilla, and a blue solid circle represents a basiconica sensilla. Scale bar = 50 μm . (B) Posterior cuticular serrations and apical teeth of *Neoplea borellii*. Scale bar = 10 μm . (C) Basiconica sensilla of *Neoplea borellii*. Scale bar = 50 μm . (D) Trichoid sensilla, designated with a yellow T, and basiconica sensilla, designated by a blue circle, on the first gonapophysis of *Neoplea borellii*. Scale bar = 10 μm .

Discussion

The immovable teeth at the apex and ventral margins of the first gonapophysis in species of *Pleididae* supports the assumption that these teeth are an adaptation for tearing into plant tissue to oviposit eggs. The saw-like form of these structures provides a functional morphology that would allow for cutting plant tissue. This is supported by the study of Atallah et al. (2014) who found that species of *Drosophila* that oviposit in plant material have similar teeth to those found in the *Pleididae* species of this study, while those *Drosophila* that lay their eggs in soft fruit lack these structures. All *Pleididae* are presumed to oviposit into plant tissue and all appear to have these teeth, with the possible exception of species in *Heteroplea* (Cook 2011), which were not included in this study. The serrated edge of the cuticle observed in *N. borellii* and *P. frontalis* are also likely to aid in cutting tissue to allow for oviposition into plant tissue. In all the pleid species in this study there were marginal teeth that were more sturdily fixed at the upper apex of the first gonapophysis, while those lower appeared somewhat flexible. The actual oviposition by pleids has not been

adequately observed to determine exactly how these teeth are used but since the generally similar arrangement of teeth is found in all of the species we observed, this appears to be an adaptation to oviposition in these species. Differences in the shape, arrangement, and number of teeth could have evolved due to the preferred host plants for oviposition although it is not known if pleid species select specific plant species for their oviposition.

All species have basiconica sensilla although the shapes differ somewhat between species. In *Paraplea* these are conical or slightly curved with a smooth surface. In *Neoplea* the basiconica sensilla are curved and somewhat conical but they all have blunt ridges. Little is known about the function of the form found in *Neoplea* but all of the basiconica sensilla are of this type, suggesting that this structure is consistent at least for *N. borellii*. Basiconica sensilla are known to aid in host plant selection in some insect species (Zhang et al. 2019). The ovipositor basiconica sensilla may have a chemosensitive role in host plant selection, but in this type, there is usually a pore associated with the sensilla (Zhang et al. 2019). The basiconica sensilla of the pleid ovipositor

does not have pores but this type is also known in other insects and is still thought to play a role in oviposition. The type of basiconica sensilla found in *Pleidae* may be mechanosensory but still used to determine a specific location for oviposition.

The trichoid sensilla are obvious mechanoreceptors but their length and arrangement has less certainty. All pleids appear to have long trichoid sensilla along the ventral surface, suggesting a common function among species. However, the role of the short trichoid sensilla observed in *P. brunni* and *N. borellii* is unclear.

It is not possible to put the results of our study into a comparative context because the ovipositors of related families have not been studied in detail by scanning electron microscopy. The ultrastructure of the closely related *Helotrephidae* and *Notonectidae* are unknown except for observations under light microscopy, however our study does show that species in *Pleidae* share some characters with at least one other group of *Hemiptera*. Although cicadas (*Cicadidae*) are distantly related *Hemiptera*, they share the general types of sensilla found in *Pleidae* (Zhong et al. 2017). Both have teeth due to their ovipositing in plant material, although the method of doing this and the structure of those teeth are quite different. Both families also have basiconica sensilla, although the shapes are again different. Cicadas also have a greater number of sensilla types, including campaniform and coeloconic sensilla. More studies, especially on groups closely related to *Pleidae*, are needed to further understand the function of these structures.

References

- Atallah, J., L. Teixeira, R. Salazar, G. Zaragoza, and A. Knopp. 2014. The making of a pest: the evolution of a fruit-penetrating ovipositor in *Drosophila suzukii* and related species. *Proceedings of the Royal Society B* 281: 20132840, 9 pp.
- Bachmann, A. O. 1968. Las Pleidae de la Republica Argentina (*Hemiptera*). *Revista de la Sociedad Entomológica Argentina* 30: 121-129.
- Benzie, J. A. H. 1989. The immature stages of *Plea frontalis* (Fieber, 1844) (*Hemiptera*, *Pleidae*), with a redescription of the adult. *Hydrobiologia* 179: 157-171.
- Cook, J. L. 2011. A new genus and species of *Pleidae* (*Hemiptera*) from Venezuela, with notes on the genera of *Pleidae*. *Zootaxa* 3067: 26-34.
- Cook, J. L., R. W. Sites, and A. Vitheepradit. 2020. The *Pleidae* (*Hemiptera*, *Heteroptera*) of Thailand, with the descriptions of two new species and a discussion of species from Southeast Asia. *ZooKeys* 973: 35-68.
- Craddock, E. M., M. P. Kambysellis, L. Franchi, P. Francisco, M. Grey, A. Hutchinson, S. Nanhoo, and S. Antar. 2018. Ultrastructure variation and adaptive evolution of the ovipositor in the endemic Hawaiian *Drosophilidae*. *Journal of Morphology* 279: 1725-1752.
- Crava, C. M., D. Zanini, S. Amati, G. Sollai, R. Crnjar, M. Paoli, M. V. Rossi-Stacconi, O. Rota-Stabelli, G. Trait, A. Haase, R. Romani, and G. Anfora. 2020. Structural and transcriptional evidence of mechanotransduction in the *Drosophila suzukii* ovipositor. *Journal of Insect Physiology* 125: 104088, 12 pp.
- Emeljanov, A. F. 2014. The evolutionary role and fate of the primary ovipositor in insects. *Entomological Review* 94: 367-396.
- Karkali, K. and E. Martin-Blanco. 2017. Mechanosensing in the *Drosophila* nervous system. *Seminars in Cell & Developmental Biology* 71: 22-29.
- Lundblad, O. 1933. Zur Kenntnis der aquatilen und semiaquatilen Hemipteren von Sumatra, Java und Bali. *Archiv für Hydrobiologie Supplement* 12: 125-145.
- Murtey, M. Das and P. Ramasamy. 2015. Sample preparations for scanning electron microscopy – life sciences. In: Janacek, M. and R. Kral eds. *Modern Electron Microscopy in Physical and Life Sciences*, eBook ISBN: 978-953-51-5063-3. 293 pp.
- Nieser, N. 1975. The water bugs (*Heteroptera* *Nepomorpha*) of the Guyana region. *Studies on the Fauna of Suriname and other Guyanas* 59: 1-310.
- Papáček, M. 2002. Morphology of the first gonapophysis and its importance for the classification of the Asian *Helotrephidae* (*Heteroptera*: *Nepomorpha*)p. 142 In *Congress Abstract of the 17th European Congress of Entomology*, Oct. 7-13, Thessaloniky, Greece.
- Papáček, M. 2008. *Esakiella* – the genus with the most ancestral first gonapophysis within the *Heloterphinae*. *Bulletin of Insectology* 61: 171-172.
- Pendegrast, J. G. 1957. Studies on the reproductive organs of the *Heteroptera* with a consideration of their bearing on classification. *Transactions of the Royal Entomological Society of London* 109: 1-63.
- Roback, S. S. and N. Nieser. 1974. Aquatic *Hemiptera* (*Heteroptera*) from the Llanos of Colombia. *Proceedings of the Academy of Natural Sciences of Philadelphia* 126: 29-49.
- Schuh, R. T. and C. Weirauch. 2020. *True Bugs of the World (Hemiptera: Heteroptera)*, Classification and Natural History (Second Edition). Siri Scientific Press, Monograph Series Volume 8, Manchester, UK. 768 pp.
- Scudder, G. G. E. 1959. The female genitalia of the *Heteroptera*: morphology and bearing on classification. *Transactions of the Royal Entomological Society of London* 111: 405-467.
- Sublett, C. A. and J. L. Cook. 2015. Morphology of the 1st gonapophysis in the genus *Neoplea* (*Hemiptera*: *Heteroptera*: *Pleidae*), including an evaluation of its taxonomic importance. *Florida Entomologist* 98: 704-713.
- Wefelscheid, H. 1212. Über die Biologie und Anatomie von *Plea minutissima* Leach. *Zoologische Jahrbücher* 32: 389-474.
- Zhang, X. S. A. H. Rizvi, H. Wang, and X. Zeng. 2019. Morphology and function of ovipositorial and tarsal sensilla of female Asian citrus psyllid. *Entomological Research* 49: 63-71.
- Zhong, H., Y. Zhang, and C. Wei. 2017. Comparative morphology of ovipositor in cicadas (*Hemiptera*: *Cicadidae*), with considerations on their taxonomic significance. *Zoomorphology* 136: 461-481.

BEAM DECELERATION ENHANCES IMAGE QUALITY OF BIOLOGICAL SAMPLES IN THE SCANNING ELECTRON MICROSCOPE

WILLIAM J. MATTHAEUS¹
AND BERND ZECHMANN^{2*}

¹Department of Biology, Baylor University One Bear Place #97388, Waco, Texas. 76798

²Center for Microscopy and Imaging, Baylor University One Bear Place #97046, Waco, Texas. 76798

*Corresponding author (Bernd_Zechmann@baylor.edu)

Abstract

Image distortions induced by the accumulation of electrons and electric fields on the surface of a specimen are commonly observed artifacts in scanning electron microscopy (SEM). This phenomenon is commonly described as charging and is especially pronounced in samples with low conductivity such as biological specimens. Charging of the surface can be reduced by applying a negative bias voltage on the sample, or the whole stage which reduces the landing energy of the beam which is called beam deceleration. This study demonstrates that the use of beam deceleration drastically reduced charging and related image distortions on butterfly wings and tobacco leaves and resulted in superior image quality.

Introduction

In scanning electron microscopy (SEM) a beam of high energy electrons scans the surface of the specimen and generates further signals that are reflected into the sample chamber. Signals include, for example, secondary electrons, backscattered electrons, x-rays, photons, and Auger electrons. These signals can then be collected by different detectors and transformed into a 2D image of the surface or chemical composition of the samples (Mignot 2018). As electrons are easily absorbed, or deflected by other molecules, beam generation and imaging is done in a vacuum to ensure that plenty of electrons are available for image generation. Some electrons from the beam, or produced by the beam on the surface of the sample, are not reflected back into the chamber of the microscope. On conductive samples (e.g. metals, carbon etc.) such electrons flow off into the ground while on samples with low conductivity (e.g. polymers, biological samples) they accumulate on the surface and build up electrical fields that lead to a phenomenon commonly described as charging (Cazaux 2004; Thiel et al., 2004; Sim et al., 2014; Flatabo 2017). Charging can result in distorted line scans, distorted ultrastructure, and bright and blurry edges. Artifacts induced by charging can be avoided by coating samples with low conductivity with a fine layer of conductive metals (e.g. gold, gold-palladium, iridium, or carbon), which allows the electrons to flow off. If not applied carefully, however, this metal coat can obscure structures of interest or build artifacts on the surface of samples (Stokross et al., 1998; Golding et al., 2016). Samples with low-conductivity can alternatively be imaged in low vacuum/variable pressure conditions (Thiel et al., 2004, Bogner et al., 2007; James 2009). Under these conditions charging is neutralized by ionized gas molecules in the specimen chamber.

An alternative approach to image specimens with low conductivity is the application of beam deceleration (Phifer et al., 2009). The sample or whole stage is held at a negative voltage which decelerates the electrons that leave the final

lens before they reach the specimen (Figure 1). The landing energy, which describes the energy of the beam when it interacts with the specimen, is determined by the initial voltage of the beam minus the stage bias voltage. Beam deceleration has been extensively used to improve image quality of material samples such as copper/palladium solder alloy, silica (Miyazaki et al., 2012; Phifer et al., 2009); and nanomaterial such as tin on carbon, diamond, gold (Miyazaki et al., 2012; Phifer et al., 2009) and polymers (Wan et al., 2009). Nevertheless, information on how this technique advances imaging capabilities of biological samples in the SEM are rare. In order to study the effects of beam deceleration on image quality of biological samples in the SEM, this study was aimed to compare the surface structure of butterfly wings and tobacco leaves observed under low and high vacuum conditions, with and without beam deceleration.

Materials and Methods

Pieces of butterfly wings from adult Gulf fritillaries (*Agraulis* sp.) were air dried and mounted on aluminum stubs with carbon tape. Some samples were sputter coated with a 15 nm layer of iridium (Leica EM ACE 600, Leica Microsystems), while other samples were imaged without sputter coating under low vacuum conditions. Samples from at least 10 different butterfly wings were analyzed for this study.

Tobacco plants [*Nicotiana benthamiana* (L.)] were cultivated in growth chambers at constant conditions of day/night temperature 22/26 °C, illumination 55 $\mu\text{mol m}^{-2} \text{s}^{-1}$, a photoperiod of 14/10 h light/dark, and a humidity of 70%. Plants were kept in pots with soil and were watered adequately. Sample preparation was carried out with an automated microwave tissue processor (Leica EM AMW; Leica Microsystems, Vienna, Austria) according to a slightly modified protocol according to Zechmann and Zellnig (2009). Small pieces (1mm²) of the youngest fully developed leaves from 5-week-old plants were cut on a wax

plate in a drop of 2.5 % glutaraldehyde in 0.06M Sorensen phosphate buffer at pH 7.2. They were then transferred into small baskets and subsequently into the chamber of the microwave processor. Fixation, buffer washes, and dehydration were then performed automatically according to the protocol described by Zechmann and Zellnig (2009). In this study osmium was not used and instead of acetone, ethanol was used during dehydration. After dehydration samples were critical point dried (Leica EM CPD 300; Leica Microsystems) with a customized program for tobacco leaves which took about 80 min (settings for CO₂ inlet: speed=medium & delay=120s; settings for exchange: speed=5 & cycles=18; settings for gas release: heat=medium & speed=medium). After critical point drying samples were mounted on aluminum stubs with carbon tape and sputter coated with 15 nm iridium (Leica EM ACE 600, Leica Microsystems). Samples were then investigated with a FEI Versa 3D scanning electron microscope (FEI, Hillsboro, OR, USA). Samples from at least 10 different leaves were analyzed for this study.

Samples were imaged at: i) high vacuum mode (about 5×10^{-6} mbar) at 5 kV; ii) high vacuum mode (about 5×10^{-6} mbar) at 3 kV; iii) low vacuum mode (1.3 mbar) at 30 kV; and ix) at high vacuum mode (about 5×10^{-6} mbar) at 5 kV with beam deceleration. When beam deceleration was used, high voltage was set to -5 kV whereas the stage bias was set to -2 kV. Thus, the electrons in the column were accelerated to 5 kV and then decelerated by 2 kV before they reached the sample with 3 kV. Therefore, the primary electrons that reached the sample had an energy of 3 kV when beam deceleration was used (Figure 1). All images were taken at a working distance of 10 mm, with a spot size of 5, a dwell time of 30 μ s, and a resolution of 1536 x 1024 pixels.

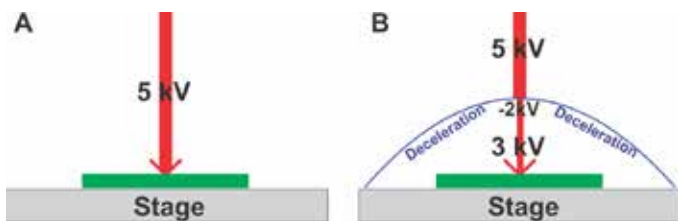


Figure 1: Schematic of beam deceleration in the SEM. A) The electron beam (red) reaches the sample (green) without beam deceleration. B) Before the electron beam (red) reaches the sample (green) it is decelerated by the negative bias voltage (blue) applied on the stage (gray). Landing energy/voltage describes the energy of the electrons when they reach the sample and is determined by the initial voltage of the beam minus the stage bias voltage of the stage. In this example the landing energy of the beam on the sample is 3kV as the original beam energy of 5 kV is decelerated by 2 kV.

Results and Discussion

Image distortions induced by charging such as shifted line scans and bright edges were commonly observed on the

surface of butterfly wings and tobacco leaves when they were imaged at high and low vacuum conditions without beam deceleration (arrows in A-C of Figures 2-5). Image quality was significantly obstructed by these effects especially at high magnification and resulted in shifted line scans (arrowheads in Figure 3B), bright (arrows in Figures 2A, B, 4A, B and 5A, B) and blurry edges (asterisks in Figure 3A) resulting in distorted ultrastructure. Coating the samples with a conductive layer of metal should have prevented these charging effects (Flatabo 2017). Nevertheless, sputter coating butterfly wings and tobacco leaves with 15 nm of iridium proved to be inefficient at preventing charging and artifacts deriving from it (A and B in Figures 2-5). Imaging uncoated butterfly wings and leaves under low vacuum also proved to be ineffective. Even though charging effects were almost completely neutralized by ionized residual gas molecules in the chamber (Miyazaki et al., 2012; Phifer et al., 2009) under low vacuum conditions, the signal to noise ratio was very low. This resulted in grainy image quality and low resolution making it difficult to image surface details of the butterfly wing scales and tobacco leaves at high magnification (C in Figures 3 and 5).

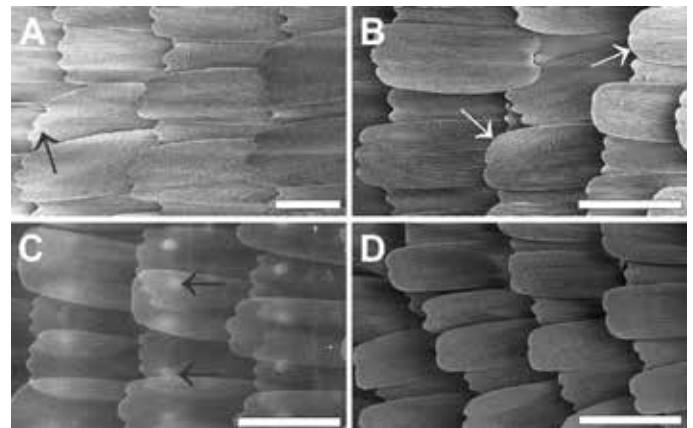


Figure 2. SEM micrographs show an overview of a butterfly wing taken at different kV settings. Images were taken at A) high vacuum mode at 5 kV, B) high vacuum mode at 3 kV, C) low vacuum mode at 30 kV, and D) high vacuum with 5 kV beam acceleration, 2 kV beam deceleration and a final beam energy on the surface of the sample of 3 kV. Samples displayed in images A, B, & D were sputter coated with 15 nm of iridium. Arrows show image distortions such as charging. Bars= 100 μ m.

Using beam deceleration under high vacuum conditions significantly improved the image quality of the butterfly wing and the leaf (D in Figures 2-5). Charging did not occur under these conditions and fine structural details on the scales of the butterfly wing (chitin lamellae) and tobacco leaves (cuticular ridges, particles) were clearly visible even at high magnifications (D in Figures 3 & 5).

The advantages of beam deceleration for imaging samples with low conductivity have already been described in some detail for material samples (Miyazaki et al., 2012;

Phifer et al., 2009; Wan et al. 2009) as well as for biological samples embedded in plastic resin (Ohta et al. 2012). The results presented in this study extend these observations

and prove that the application of beam deceleration leads to superior image quality of biological samples in the SEM when compared to samples imaged at high and low vacuum without beam deceleration.

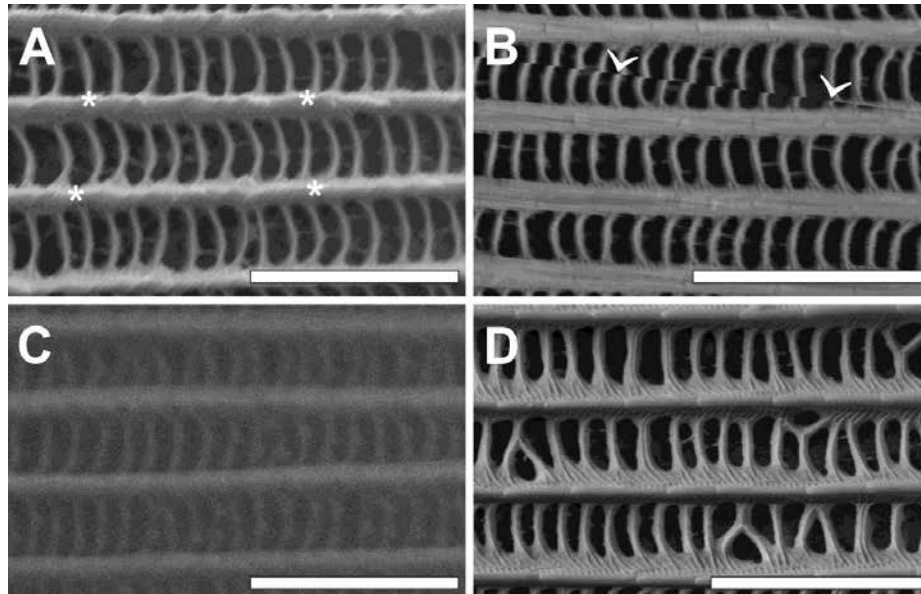


Figure 3. SEM micrographs show a close up of a scale of a butterfly wing taken at different kV settings. Images were taken at A) high vacuum mode at 5 kV, B) high vacuum mode at 3 kV, C) low vacuum mode at 30 kV, and D) high vacuum with 5 kV beam acceleration, 2 kV beam deceleration and a final beam energy on the surface of the sample of 3 kV. Samples displayed in images A, B, & D were sputter coated with 15 nm of iridium. Image distortions such as blurry edges (asterisks) and shifted line scans (arrowheads) were commonly observed in samples imaged without beam deceleration. Bars= 5 μ m.

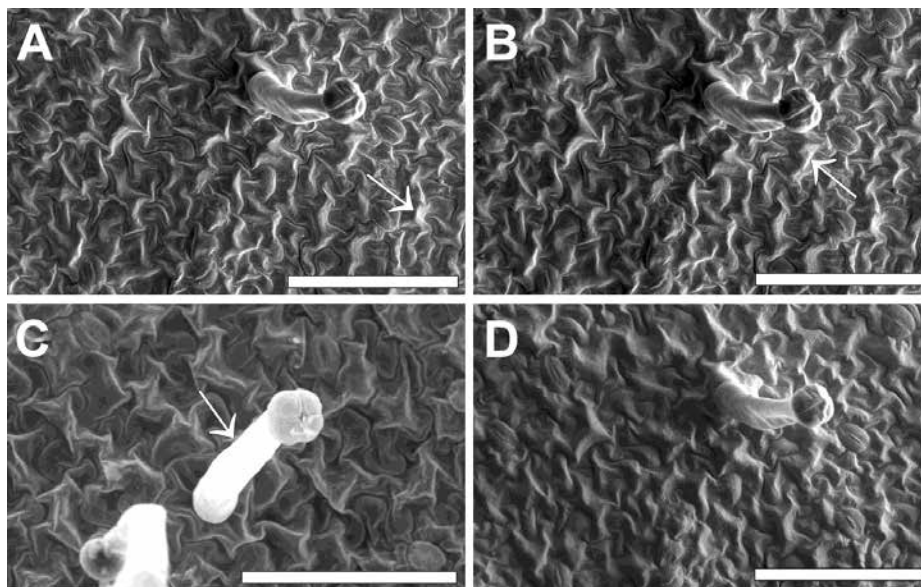


Figure 4. SEM micrographs show an overview of a leaf from *Nicotiana benthamiana* taken at different kV settings. Images were taken at A) high vacuum mode at 5 kV, B) high vacuum mode at 3 kV, C) low vacuum mode at 30 kV, and D) high vacuum with 5 kV beam acceleration, 2 kV beam deceleration and a final beam energy on the surface of the sample of 3 kV. Samples displayed in images A, B, & D were sputter coated with 15 nm of iridium. Arrows show image distortions such as charging. Bars= 100 μ m.

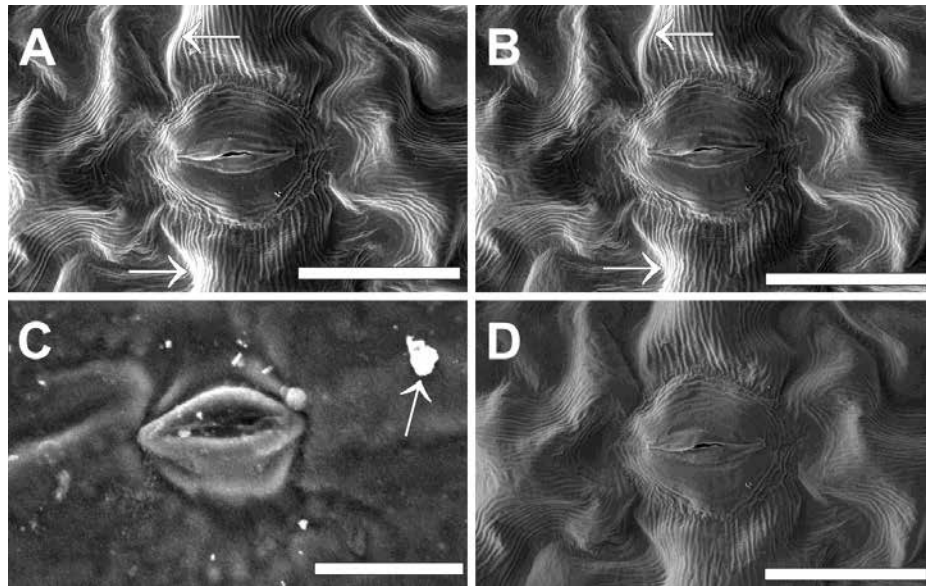


Figure 5. SEM micrographs show a close up of stomata on a leaf of *Nicotiana benthamiana* taken at different kV settings. Images were taken at A) high vacuum mode at 5 kV, B) high vacuum mode at 3 kV, C) low vacuum mode at 30 kV, and D) high vacuum with 5 kV beam acceleration, 2 kV beam deceleration and a final beam energy on the surface of the sample of 3 kV. Samples displayed in images A, B, & D were sputter coated with 15 nm of iridium. Arrows show image distortions such as charging, blurry edges, and shifted structures. Bars= 20 μm .

Conclusion

Beam deceleration under high vacuum proved to be the most efficient method to image fine structural surface details of butterfly wings and tobacco leaves in the SEM. Artifacts such as charging, commonly observed at low and high vacuum conditions without beam acceleration, were diminished when beam deceleration was used resulting in superior image quality.

References

- Bogner, A., Jouneau, P.H., Thollet, G., Basset D. and Gauthier C., 2007. A history of scanning electron microscopy developments: Towards “wet-STEM” imaging. *Micron* 38:390-401.
- Cazaux, J., 2004. Charging in Scanning Electron Microscopy “from Inside and Outside”. *Scanning* 26:181-203.
- Flatabø, R., Coste, A. and Greve, M.M., 2017. A systematic investigation of the charging effect in scanning electron microscopy for metal nanostructures on insulating substrates. *Journal of Microscopy* 265:287-297.
- Golding, C.G., Lamboo, L.L., Beniac, D.R. and Booth, T.F., 2016. The scanning electron microscope in microbiology and diagnosis of infectious disease. *Scientific Reports* 6: 26516.
- James, B., 2009. Advances in “wet” electron microscopy techniques and their application to the study of food structure. *Trends in Food Science & Technology* 20:114-124.
- Kim, K.H., Akase, Z., Suzuki, T. and Shindo, D., 2010. Charging effects on SEM/SIM contrast of metal/insulator system in various metallic coating conditions. *Materials Transactions* 51:1080-1083.
- Mignot C., 2018. Color (and 3D) scanning electron microscopy. *Microscopy Today* 26:12-17.

- Miyazaki, H., Uosaki, H., Tojo, A., Hirashima, S., Inaga, S., Sakuma, K., Morishita, Y. and Fukayama, M., 2012. Application of low-vacuum scanning electron microscopy for renal biopsy specimens. *Pathology – Research and Practice* 208:503-509.
- Ohta, K., Sadayama, S., Togo, A., Higashi, R., Tanoue, R. and Nakamura, K., 2012. Beam deceleration for block-face scanning electron microscopy of embedded biological tissue. *Micron* 43:612-620.
- Phifer, D., Tuma, L., Vystavel, T., Wandrol, P. and Young, R.J., 2009. Improving SEM imaging performance using beam deceleration. *Microscopy Today* 17:40-49.
- Sim, K.S., Tan, Y.Y., Lai, M.A., Tso, C.P. and Lim, W.K., 2010. Reducing scanning electron microscope charging by using exponential contrast stretching technique on post-processing images. *Journal of Microscopy* 238:44-56.
- Stokroos, I., Kalicharan, D., Van der Want, J.J.L. and Jongebloed, W.L., 1998. A comparative study of thin coatings of Au/Pd, Pt and Cr produced by magnetron sputtering for FE-SEM. *Journal of Microscopy* 189:79-89.
- Thiel, B.L., Toth, M. and Craven J.P., 2010. Charging processes in low vacuum scanning electron microscopy. *Microscopy and Microanalysis* 10:711-720.
- Wan, Q., Masters, R.C., Lidzey, D., Abrams, K.J., Dapor, M., Plenderleith, R.A., Rimmer, S., Claeysens, F. and Rodenburg, C., 2016. Angle selective backscattered electron contrast in the low-voltage scanning electron microscope: Simulation and experiment for polymers. *Ultramicroscopy* 171:126-138.
- Zechmann B. and Zellnig G., 2009. Microwave assisted rapid plant sample preparation for transmission electron microscopy. *Journal of Microscopy* 233:258-268.

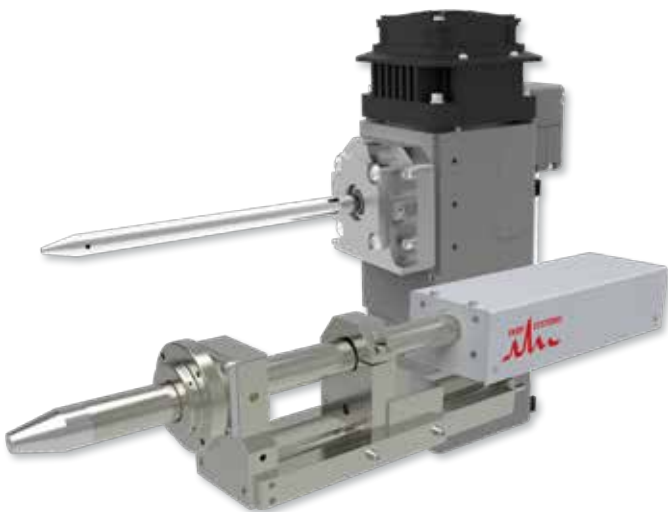


Enhance your SEM / TEM with full-spectrum elemental analysis !

Beyond our full suite of EDS/XRF hardware including detectors, digital pulse processors, microXRF spectrometers and X-ray sources, we offer **Iridium Ultra** software recognized as the best in the industry by expert users:



Top spectra is e-beam excitation, bottom spectra is X-ray excitation.



SEM-XRF X-ray sources. micro X-ray source with polycapillary optic (top) delivers a 10 μ m spot. Small spot XRF source (bottom) produces a 200 μ m spot.

Why add an X-ray source to your SEM-EDS ?

- Analyze all elements
 - Beryllium (Be) to uranium (U)
- Trace level analysis
 - Sodium (Na) through uranium (U)
 - With a micro X-ray source
- Fits most any microscope

Serving the electron microscopy community for 28 years, we are your Central Texas neighbors:



IXRF, Inc. • 10421 Old Manchaca Rd., Ste. 620 • Austin, TX 78748 USA
www.ixrfsystems.com • info@ixrfsystems.com
P: +1 512.386.6100 • F: +1 512.386.6105
[LinkedIn.com/company/ixrf-systems](https://www.linkedin.com/company/ixrf-systems)



MATERIAL SCIENCES

Spring 2021

IN-SITU MAGNETIZATION MAPPING OF THE MAGNETIC EVOLUTION IN NI NANOWIRES BY ELECTRON HOLOGRAPHY

ARTURO GALINDO, ANDREI HERNANDEZ-ROBLES, EDUARDO ORTEGA, JASON GIULIANI,
AND ARTURO PONCE*

Department of Physics and Astronomy, University of Texas at San Antonio, One UTSA Circle, San Antonio, TX, 78249,
USA.

*Corresponding Author (arturo.ponce@utsa.edu)

Abstract

The magnetization reversal mechanism in Nickel (Ni) nanowires was studied under external magnetic fields of 50 - 4100 Oe through an electron holography experiment. Initially, a modified analytical transmission electron microscopy (TEM) holder was adapted into a Hall sensor to measure the remnant magnetic field produced by the objective lens (OL), which was characterized at about 45 Oe for a JEOL ARM 200F. Subsequently, the magnetic field strength produced by the OL was measured as a function of the excitation voltage. The acquired field measurements were used to systematically increase the magnetic field to demonstrate the evolution of the in-plane magnetic flux, magnetic induction, and the stray magnetic field lines within and around an individual nanowire and a single row of nanowires by acquiring holograms successively at different stages of the magnetization reversal process. This capability employs interferometric principles to achieve a nanometric spatial resolution combined with a quantitative and qualitative experimental approach to probe the full magnetic spectrum under dynamic magnetic field environments.

Introduction

With the rapid development of information storage technology, increasing interest in magnetic nanomaterials has inspired a great deal of research in recent years. The micromagnetic behavior in materials, like other physical properties, is modified when a material is confined to the nanoscale. For this reason, various techniques to fabricate ferromagnetic (FM) nanowires have been greatly investigated as they offer unique advantages in developing high-density magnetic recording media (Kou et al., 2011). It is well known that their miniaturized dimensions at the nanoscale generate anisotropic properties that differ from the physical properties of bulk materials due to a competing energy balance between the shape and crystallographic structure in the nanowires (Carignan et al., 2007). Consequently, the precise control of the magnetic properties of high-dense arrays of FM nanowires is a great challenge in nanotechnology.

Transmission electron microscopy (TEM) has more than ten different modes of operation and associated techniques with it. There are dedicated specialized modes such as environmental microscopes designed to perform chemical reactions *in-situ* TEM and designs to irradiate samples with low doses and work in cryogenic conditions. However, a microscope dedicated to studying the magnetic and electrostatic properties in nanomaterials has not been conveyed. Thus far, the magnetic state of nanomaterials can be imaged using various techniques such as magnetic force microscopy and Kerr microscopy (Liu et al., 2008; Pimentel et al., 2007); however, the magnetic information obtained

is limited to the exterior of the nanomaterial. In contrast, a powerful magnetometry measurement tool with high spatial resolution rests in a specialized TEM mode called off-axis electron holography. This technique is equipped to visualize and quantify the local magnetic configuration within and around a magnetic nanomaterial by employing a Möllenstedt biprism located beneath the OL (Möllenstedt & Düker, 1955).

Attempts to design a microscope dedicated to off-axis electron holography have been highlighted in the last decade with the construction of a multiple biprism microscope. One of the great advancements has been the development of new ultrasensitive electron detectors that are designed to recover the phase of images or diffraction patterns such as phase differential contrast and 3D electron ptychography (Lupini et al., 2018). Nevertheless, a commercial TEM dedicated to off-axis electron holography that automatically provides the illumination conditions for optimized phase resolution is lacking. Therefore, the acquisition and optimization of images must be performed manually. One of the operating principles for this type of microscope is based on dynamically adapting the field of view by adding lenses below the sample and adjusting the electric potential administered to the biprism at different magnifications. In the same fashion, one of the recently proposed designs suggests adding a lens below the sample before the biprism (Voelkl, 2019). This design counteracts the high magnetic field produced by OL and permits measurements of the intrinsic electrostatic potential and magnetic induction in FM nanostructures before reaching their magnetic saturation state.

The study of magnetic domains or magnetic flux is not a straightforward method in TEM, one needs a phase retrieval method to deduce the magnetic flux inside and outside the samples. Electron holography permits the phase retrieval of electron waves once a voltage is administered to the biprism. Consequently, the electron waves traveling simultaneously through a vacuum and sample region overlap and generate interference fringes at the detector screen to record holograms. The basis for holography lies in the comprehension of interferometry, which studies how wavefronts are combined in space at a given time. The holographic work presented by Dennis Gabor (Gabor, 1949) has proven to be the first interferometric experiment using electrons which has then been improved for the past three decades by using field emission filaments to produce highly coherent electron waves.

In off-axis electron holography, a major limitation is the OL which applies an external magnetic field higher than 15 kOe. The applied magnetic field is large enough to saturate most magnetic nanostructures making it difficult to observe their spontaneous magnetic state. This work aims to investigate the magnetization process of Ni nanowires by using off-axis electron holography to isolate the local magnetic induction as a function of an applied external magnetic field generated by the OL. Imaging the magnetic state at various magnetic field strengths offers the most detailed look at the magnetization process that occurs within Ni nanowires.

Materials and Methods

We employed off-axis electron holography to perform *in-situ* magnetization measurements on individual and an array of Ni nanowires. Electrochemical depositions were performed in a three-electrode configuration by employing an anodic aluminum oxide template (AAO) as the working electrode, a platinum mesh counter electrode, and an Ag/AgCl reference electrode. All electrodepositions were performed using a commercial Nickel Sulfamate RTU (Technic Inc. 47 Molter Street Cranston, Rhode Island 02910, USA) solution at a pH of 4.01. Moreover, the AAO was removed by exposing the sample to a solution of 0.5 M NaOH for 2 h. Subsequently, the nanowires were sonicated and collected in a TEM grid (lacey carbon 300 mesh on Cu). Additionally, a row of nanowires was etched with gallium ions using a Focused Ion Beam (FIB) Carl Zeiss model Crossbeam 340 operated at 30, 5, and 2 kV to avoid damage. The nanowires exhibit a high aspect ratio with a diameter of 80 nm and length of $\sim 1 \mu\text{m}$ to promote a strong shape anisotropy in the longitudinal direction of the nanowire.

The magnetic field produced by the OL was characterized via an *in-situ* setup using a Hall Effect sensor positioned at the specimen region within the TEM column (Ponce-Pedraza et al., 2019). The Hall effect sensor is a transducer that varies its output voltage in response to an alternating magnetic field. As a transducer, the sensor converts the magnetic energy into an electric signal. The output is then sent to a Gaussmeter that quantifies the magnetic field

measured. After inserting the Hall effect sensor into the TEM column, the OL voltage was gradually increased to measure the magnetic field produced with a Gaussmeter (Schofield et al., 2008). To calibrate the magnetic contribution inside the TEM column, an analytical TEM holder was modified as shown in the inset of Figure 1A. The Hall probe was adapted in an analytical commercial holder from Nanofactory Instruments. The four connections of the Hall sensor were welded to the chip channels to avoid additional wiring. The holder outputs were connected directly to the Gaussmeter Hall Effect sensor model HSU-1 and a Hall Effect Gaussmeter Model GM-700 from Cryomagnetics, Inc. The sensor active area was $0.1 \times 0.1 \text{ mm}$ with an overall dimension of $4 \times 5 \times 1 \text{ mm}$.

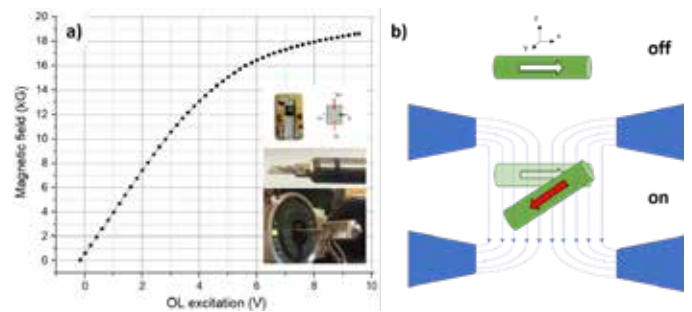


Figure 1. Magnetic field produced in the specimen position. A) Magnetic field produced in the specimen position as a function of the OL excitation voltage. B) Two conditions are illustrated: Lorentz conditions (no magnetic field produced by the OL) prevail in the off state while a magnetic field is produced in the “on” state. The sample is tilted with respect to the optical axis. The tilting angle determines the direction of magnetization.

A steady measurement of 60.7 G was recorded before introducing the Hall sensor in the TEM column (Ponce-Pedraza et al., 2019). Once the Hall sensor was at the sample position, the magnetic field measurement initiated with the OL turned off to resemble the Lorentz conditions. A remanent field of $\sim 45 \text{ Oe}$ was evaluated in this arrangement. Henceforth, the applied voltage of the OL was increased from -0.17 V to 9.55 V by increments of 0.2 V as seen in Figure 1A. After the voltage saturation was reached a reversal process was performed to restore the initial voltage conditions. The residual magnetic field of the OL was measured at $\sim 50 \text{ Oe}$ (the trajectory of the magnetic field lines is illustrated in Figure 1B). Other microscopes have reported minor remanent fields measuring at 4 Oe (Lau et al., 2007). For instance, L.A. Rodriguez et al. performed Lorentz microscopy and electron holography experiments to study the dynamics of domain walls in $\text{Co}_{50}\text{Fe}_{50}$ nanowires under a remanent field of 30 Oe (Rodríguez et al., 2013). The reason for the large field variation is due to the different designs of the pole piece within each microscope. In essence, the magnetic measurements during the specimen loading procedure were very stable and no variations were detected. The measurement was

reproducible after applying a relaxation process to the lenses and an error was determined in the range of 0.25-0.35%. In this way, systematic studies can be performed via *in-situ* TEM by using the OL as an external magnetic field source.

In electron holography, the interference of the magnetic vector within a magnetic nanowire produces a phase shift in the electron wave function that travels through the sample following the principles of the Aharonov-Bohm effect (Aharonov & Bohm, 1961). In this way, we can describe the total phase recovered (φ Total) as the convolution of several contributions denoted by φ Total= φ E+ φ M where φ E and φ M represent the electrostatic (includes the mean inner potential) and the magnetostatic components, respectively. In this way, the reconstructed phase provides mutual information as described in the following equation (Cantu-Valle et al., 2015):

$$\varphi_{Total}(x, y) = C_E \int V(x, y, z) \cdot dz - \frac{e}{\hbar} \iint B_{\perp}(x, y) \cdot dx \cdot dz$$

(Equation 1)

where C_E is an energy-dependent constant determined by the acceleration voltage. Hence, for the energy of 200 kV (used in this experiment), a value of 0.00729 rad/ (V·nm) was determined. As a result, the phase shift can be detected and evaluated quantitatively provided that the electrostatic and magnetostatic phases are separated. Only then can the reconstructed phase be evaluated quantitatively. The phase reconstruction was carried out using the script HoloWorks 5.0.7 in Digital Micrograph software (Volk et al., 1995).

Furthermore, the holograms were collected using the optimal conditions in a JEOL ARM 200F microscope. A fringe contrast of $\mu = 56\%$ and fringe spacing of $\sigma = 10.6$ nm were obtained from the interference fringes positioned parallel to the nanowires. To isolate the pure magnetic contribution to the recorded phase change, the sample stage was tilted $\pm 16^\circ$ as seen in Figure 1B. As the maximum tilt angle was reached, the OL was turned on at each maximum position to apply a magnetic field perpendicular to the sample stage and induce a magnetization reversal mechanism. The holograms were acquired after the OL was turned off and the sample stage was returned to 0° . Following Equation 1, a digital subtraction process was executed on the complex phase images to eliminate the phase change associated with the mean inner potential (electrostatic contribution). Therefore, as the voltage administered to the OL was increased, a quantitative evaluation of the remnant magnetic induction (\vec{B}) and magnetization (\vec{M}) values within the nanowire were experimentally obtained from the reconstructed phase images (see Table 1). In the same way, the magnetostatic contribution was maintained at a constant amplification of 7x the cosine of the unwrapped magnetic phase to allow comparison at different stages of the magnetization process. Since the magnetic contour images have a direct correspondence to the enclosed magnetic flux in the nanowire, we observed the magnetic flux evolution in

response to an increasing external magnetic field, which is visually aided by the color wheel as it illustrates the direction of propagation. Moreover, the crystal orientation mapping was performed using an automated crystal orientation system that employs a precession electron diffraction unit manufactured by Nanomegas. The applied probe size was 2 nm, and a total area of 400 nm x 1,200 nm was analyzed. Each diffraction pattern was acquired at a speed of 0.04 s per frame.

OLv	H (Oe)	$\Delta\phi$ (rad)	\vec{M}	\vec{B}
0.1	980	4.25	3.44E+05	0.49
0.2	1320	4.5	3.64E+05	0.51
1	4100	7	5.67E+05	0.65

Table 1. Measured magnetic fields generated by the voltage sequence applied to the OL. The calculated M and B values are shown per the measured phase change ($\Delta\phi$) from the electron holography experiments.

Results & Discussion

For an isolated Ni nanowire, the spontaneous magnetic state is portrayed as a continuous magnetic flux with an undulating behavior within the nanowire as seen in Figure 2B. The wavy propagation emerges from the misorientation of the crystal grains at the grain boundaries as the flux direction alternates between 0° and 45° , despite the larger grains detected along the longitudinal axis. Therefore, the overall magnetic flux direction is maintained along with the shape of the nanowire. However, once the magnetic flux reaches the tip a sequence of vortex states is generated. This is explained by the varying sizes and orientations of the crystal grains observed in Figure 2A. The polycrystalline structure at the tip decreases the magnetocrystalline anisotropy energy and induces a drift to the magnetic flux, thus reversing the direction of propagation via a curling mode. The 180° rotation observed in the midsection (highlighted by the green and pink colors) is an indication of the minimization of energy within the nanowire to stabilize and maintain a magnetic state of lowest energy. Additionally, the absence of voids and the continuous display of the magnetic flux lines are indicative of the dominant shape anisotropy that orients the magnetic flux along the nanowire long axis. Furthermore, the stray field lines observed outside the nanowire suggest the existence of magnetic domain walls oriented perpendicular to the long axis of the nanowire (Gatel, 2020). This behavior is thought to be influenced by the combination of the misoriented transverse crystal grains and the slight remnant field from the OL (~ 50 Oe) applied perpendicular to the nanowire. The number of stray field lines represents the magnetic variation in the nanowire for which 6 green lines were counted.

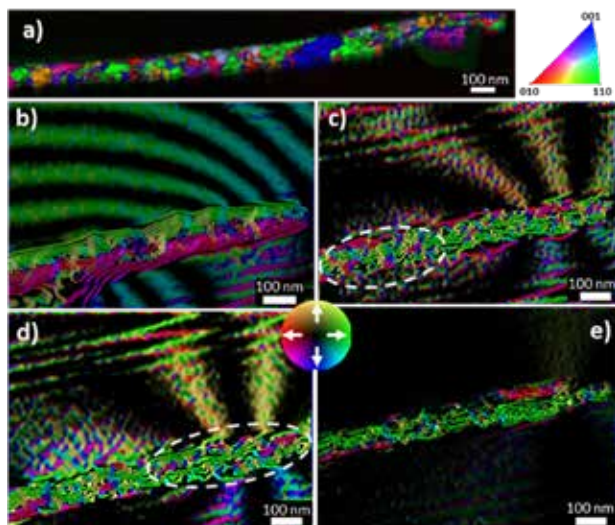


Figure 2. TEM images displaying crystal orientation map of a Ni nanowire concerning the z-axis (parallel to the electron beam path) (A). The color code specifies the presence of (111), (110), or (010) crystal phases for fcc Ni. B) – E) Magnetic phase contour maps of a Ni nanowire exposed to an external magnetic field strength of 50, 980, 1320, and 4100 Oe, respectively. All magnetic contour maps were amplified by 7X the cosine of the unwrapped magnetic phase. The regions circled by the white-dash line highlights the evolution of the vortex cores. The arrows on the color wheel show the propagation direction of the magnetic flux.

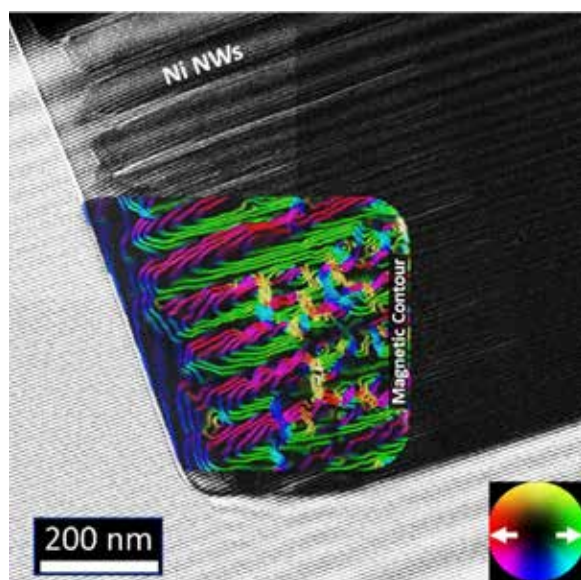


Figure 3. Electron hologram of a single row of Ni nanowires displaying the overlapped interference fringes in a TEM. The colored inset displays the reconstructed magnetic phase contour amplified at 3X the cosine of the unwrapped magnetic phase. Magnetic flux direction is indicated by the color wheel.

Correspondingly, as the OL voltage was increased to 0.1 V a magnetic field of 980 Oe was applied to the sample stage. The adjacent magnetic flux lines propagating at 180° observed in Figure 2B were replaced by a unidirectional magnetic flux oriented along the longitudinal axis represented by the prevailing green color in Figure 2C. It is noted that for Ni nanowires of 80 nm diameter the magnetization reversal mechanism is dominated by the propagation of vortex cores along the longitudinal axis of the nanowire (Hertel & Kirschner, 2004). Therefore, as highlighted at the base of the nanowire various vortex cores were observed rotating in a clockwise orientation. As the magnetic field increased to 1320 Oe (Figure 2D) the position of the vortex cores was shifted to the tip of the nanowire suggesting a propagation of the cores along the nanowire. Note that the vortex cores rotate perpendicularly to the nanowire axis. Hence, the stray fields observed in Figures 2C and 2D characterized as 3 and 2 lines, respectively, emanate from the uncompensated flux closure of the vortex cores as opposed to magnetic domain walls. This magnetic behavior became evident once a field strength of 4100 Oe was administered (Figure 2E). The vortex cores disappeared along with the stray field lines previously observed outside the nanowire. This indicates that the magnetic saturation state for a single nanowire was reached as the magnetic flux became uniform with minor changes in direction. The values for the magnetic saturation and magnetic induction were evaluated from a phase change of 7 rad (Cantu-Valle et al., 2015). The experimental values were obtained from Figure 2E which correspond to a magnetic saturation of $M_s = 5.6 \times 10^5$ A/m and a magnetic induction of $B = 0.65$ T which agrees with reported values for Ni nanowires (Drisko et al., 2018; Ortega et al., 2018). This result is consistent with the described magnetization reversal mechanism.

Comparatively, the magnetic flux response of a single row of Ni nanowires with 80 nm diameter was directly visualized using off-axis electron holography. Figure 3 presents the electron hologram of the single row of Ni nanowires after being prepared by FIB. The hologram collecting conditions were $\mu = 35\%$ and $\sigma = 12.5$ nm. Moreover, the registered holograms were obtained after tilting the sample stage at 21.2° and applying a magnetic field of 16,500 Oe perpendicular to the longitudinal axis of the nanowires. The reconstructed magnetic phase is displayed as the colored inset in Figure 3 where the magnetic contour displays a direct visualization of the magnetostatic interactions among a single row of Ni nanowires. Although, a relatively high magnetic field was employed in this experiment, a state of magnetic saturation was not achieved. The prevailing green and purple colors demonstrate that the magnetic flux is oriented at 132° within each nanowire. In contrast to an isolated nanowire, the high packing factor promotes strong magnetostatic coupling and dipolar interactions as the magnetic flux movement journeys into the adjacent nanowires at the tip and middle areas. This analysis shows the complexity of magnetic interactions introduced by the spatial distribution of Ni nanowires in AAO templates.

Conclusion

Sequential *in-situ* reversal magnetization measurements were performed on Ni nanowires by using the OL within the TEM column as an external magnetic field source. At the sample position, the magnetic field strength and remanent field from the OL were characterized by a Hall sensor that was modified from an analytical TEM holder. Experimental evidence of the magnetic flux evolution in and around the nanowire in response to an increasing magnetic field was registered by using off-axis electron holography. We showed how the reconstructed magnetic phase contours provide qualitative results that helped identify the nature of the magnetization reversal mechanism prevailing in the nanowire. In the same way, the magnetic induction within the NW was extracted at various stages of the magnetic field increment as the phase shift of the electron wave was evaluated accordingly. Furthermore, the magnetostatic interactions amongst neighboring nanowires of 80 nm diameter were qualitatively evaluated through the magnetic flux movement. As can be seen, the resolving power of electron holography was demonstrated as a TEM technique that utilizes the concealed physical information hidden within the phase shift of the electron wave to elucidate the hidden properties of nanomaterials.

Funding

This work was funded by a Research Development and Engineering Command of the United States Department of Defense grant W911NF-18-1-0439.

References

- Aharonov, Y., & Bohm, D. (1961). Significance of Electromagnetic Potentials in the Quantum Theory. *Physical Review*, 123(4), 1511–1524.
- Cantu-Valle, J., Díaz Barriga-Castro, E., Vega, V., García, J., Mendoza-Reséndez, R., Luna, C., Manuel Prida, V., Nielsch, K., Mendoza-Santoyo, F., Jose-Yacaman, M., & Ponce, A. (2015). Quantitative magnetometry analysis and structural characterization of multisegmented cobalt-nickel nanowires. *Journal of Magnetism and Magnetic Materials*, 379, 294–299.
- Carignan, L. P., Lacroix, C., Ouimet, A., Ciureanu, M., Yelon, A., & Ménard, D. (2007). Magnetic anisotropy in arrays of Ni, CoFeB, and Ni/Cu nanowires. *Journal of Applied Physics*, 102(2).
- Drisko, G. L., Gatel, C., Fazzini, P. F., Ibarra, A., Mourdikoudis, S., Bley, V., Fajerweg, K., Fau, P., & Kahn, M. (2018). Air-Stable Anisotropic Monocrystalline Nickel Nanowires Characterized Using Electron Holography. *Nano Letters*, 18(3), 1733–1738.
- Gabor, D. (1949). Microscopy by reconstructed wave-fronts. *Proc Roy Soc Ser A Math Phys Sci*, 197(1051).
- Gatel, C. (2020). Quantitative field mapping at the nanoscale by transmission electron microscopy. Doctoral Dissertation Université Paul Sabatier Toulouse III.
- Hertel, R., & Kirschner, J. (2004). Magnetization reversal dynamics in nickel nanowires. *Physica B: Condensed Matter*, 343(1–4), 206–210.
- Kou, X., Fan, X., Dumas, R. K., Lu, Q., Zhang, Y., Zhu, H., Zhang, X., Liu, K., & Xiao, J. Q. (2011). Memory effect in magnetic nanowire arrays. *Advanced Materials*, 23(11), 1393–1397.
- Lau, J. W., Schofield, M. A., & Zhu, Y. (2007). A straightforward specimen holder modification for remnant magnetic-field measurement in TEM. *Ultramicroscopy*, 107(4–5), 396–400.
- Liu, Z., Chang, P. C., Chang, C. C., Galaktionov, E., Bergmann, G., & Lu, J. G. (2008). Shape anisotropy and magnetization modulation in hexagonal cobalt nanowires. *Advanced Functional Materials*, 18(10), 1573–1578.
- Lupini, A. R., Oxley, M. P., & Kalinin, S. V. (2018). Pushing the limits of electron ptychography. *Science*, 362(6413), 399–400.
- Möllenstedt, G., & Düker, H. (1955). Fresnel'scher Interferenzversuch mit einem Biprisma für Elektronenwellen. *Die Naturwissenschaften*, 42(2), 41.
- Ortega, E., Santiago, U., Giuliani, J. G., Monton, C., & Ponce, A. (2018). In-situ magnetization/heating electron holography to study the magnetic ordering in arrays of nickel metallic nanowires. *AIP Advances*, 8(5).
- Pimentel, P. M., Leven, B., Hillebrands, B., & Grimm, H. (2007). Kerr microscopy studies of microwave assisted switching. *Journal of Applied Physics*, 102(6).
- Ponce-Pedraza, A., Yacaman, J., & Sanchez, J. E. (2019). U.S Patent 10,373,801 B2.
- Rodríguez, L. A., Magén, C., Snoeck, E., Gatel, C., Marín, L., Serrano-Ramón, L., Prieto, J. L., Muñoz, M., Algarabel, P. A., Morellón, L., De Teresa, J. M., & Ibarra, M. R. (2013). Quantitative in situ magnetization reversal studies in Lorentz microscopy and electron holography. *Ultramicroscopy*, 134, 144–154.
- Schofield, M. A., Beleggia, M., Zhu, Y., & Pozzi, G. (2008). Characterization of JEOL 2100F Lorentz-TEM for low-magnification electron holography and magnetic imaging. *Ultramicroscopy*, 108(7), 625–634.
- Voelkl, E. (2019). Electron Holography for Everyone - Here It Comes. *Microscopy Today*, 27(1), 34–35.
- Volk, E., Allard, L. F., & Frost, B. (1995). A software package for the processing and reconstruction of electron holograms. *Journal of Microscopy*, 180(1), 39–50.

JOIN THE TEXAS SOCIETY FOR MICROSCOPY ON SOCIAL MEDIA



Follow us on Facebook (<https://www.facebook.com/Texas-Society-for-Microscopy-214124248659260>) and Twitter (<https://twitter.com/MicroscopyTexas>)

Home About Events Photos Me

About See all

TSM Mission Statement: The purpose of this Society is to further the use, understanding, and knowledge of all aspects of microscopy and their applications as they apply to life sciences, materials sciences and industry. [See less](#)

187 people like this including 1 of your friends

202 people follow this

<http://www.texasmicroscopy.org/index.html>

Send message

texasocietyformicroscopy@yahoo.com

Nonprofit Organization



THE TEXAS SOCIETY FOR MICROSCOPY
February 20th - 22nd, 2020

Abstract Submission

Abstract Deadline: We are pleased to announce the abstract submission deadline for the 55th meeting is **February 13, 2020**. Abstracts should be submitted to: abstracts@texasmicroscopy.org.

Abstract Topic: There will be no restriction on abstract topics. The TSM will accept abstracts in all areas of microscopy, including but not limited to: Life Sciences, Materials Science, and Industry.

Abstract Length: Abstracts should be limited to 250 words. The TSM will accept abstracts in all areas of microscopy, including but not limited to: Life Sciences, Materials Science, and Industry.

Abstract Format: Abstracts should be submitted in PDF format. The TSM will accept abstracts in all areas of microscopy, including but not limited to: Life Sciences, Materials Science, and Industry.

THE TEXAS SOCIETY FOR MICROSCOPY
"Furthering all fronts of Microscopy"
February 20th through 22nd, 2020
Texas A&M University-Corpus Christi
College Station, Texas

Registration will be held at the Microscopy and Imaging Center and the Materials Science Building, Texas A&M University-Corpus Christi

General C&I Fee Waiver: All members are encouraged to present their research in an oral or poster format. The TSM will accept abstracts in all areas of microscopy, including but not limited to: Life Sciences, Materials Science, and Industry.

Registration Information: Registration information is available on the TSM website. The TSM will accept abstracts in all areas of microscopy, including but not limited to: Life Sciences, Materials Science, and Industry.

Abstract Submission: Abstract submission information is available on the TSM website. The TSM will accept abstracts in all areas of microscopy, including but not limited to: Life Sciences, Materials Science, and Industry.

Abstract Deadline: Abstract submission deadline is February 13, 2020. The TSM will accept abstracts in all areas of microscopy, including but not limited to: Life Sciences, Materials Science, and Industry.

The 55th Texas Society for Microscopy Meeting February 20-22, 2020, College Station, TX





Embracing All Forms of Microscopy

Welcome to the Texas Society for Microscopy

About Us

The Texas Society for Microscopy (TSM) was founded in 1963 and has become an informative resource for many scientists since then. We welcome microscopists, researchers, students and administrators from all disciplines and backgrounds who are interested in microscopy or the science of microscopy.

Our non-profit organization is committed to advancing knowledge and understanding of all aspects of microscopy and their applications as they apply to life sciences, materials sciences and industry. We are committed to support students through our **Small Grant Program** and through travel grants to attend our annual meetings. The society is also represented at the meetings of the Microscopy Society of America through our president. The annual meetings of the TSM are a highlight for our members and enjoy wide corporate support.

We invite you to become a member of the TSM and support its mission and vision through your **membership**.

Upcoming Meetings



2022 TSM Meeting - March 24, 2022 9:00 am



THE TEXAS JOURNAL OF MICROSCOPY IS AVAILABLE ONLINE



Advancing Microscopy and Microanalysis



Embracing All Forms of Microscopy

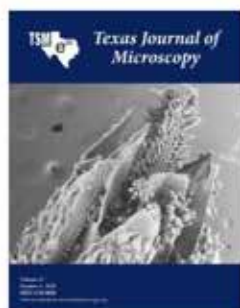
[HOME](#) [ABOUT](#) [MEMBERSHIP](#) [EVENTS](#) [SMALL GRANT](#) [JOURNAL](#) [CONTACT US](#)



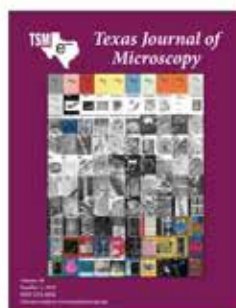
Texas Journal of Microscopy

The "Texas Journal of Microscopy" is the official journal of the Texas Society for Microscopy (TSM), which is committed to advancing knowledge and understanding of all aspects of microscopy and its application as it applied to life sciences, material sciences and industry. We welcome the submission of scientific papers covering theory, design, methods, application, and practice of microscopy and microanalysis in all fields of life sciences, material sciences, nanotechnology and engineering. Original publications, review articles, and short communications are welcome. Manuscripts will be considered for publication only if they have not been published, or submitted elsewhere, and have passed the peer-review process of suitable reviewers. The "Texas Journal of Microscopy" is an open access journal. Additionally, a print version of the journal is published annually which contains all accepted articles and the abstracts of the annual meeting of the TSM. While non-members will be charged a \$200 processing fee for each published article, publication is free for members of the TSM.

Most Recent Issues:



Vol. 51-1 (2020)



Vol. 50-1 (2019)

Archive:

- Volumes 41-50 (2010-2019)
- Volumes 31-40 (2000-2009)
- Volumes 21-30 (1990-1999)
- Volumes 11-20 (1980-1989)
- Volumes 2-10 (1970-1979)
- Volume 1 (1967-1970)

CALL FOR PAPERS

Authors are invited to submit their manuscripts for the next edition of the Texas Journal of Microscopy. The objective of the journal is to publish papers on original research and development of methods for providing prospect guidelines to research supported by all forms of microscopy. Please send your work as short communications, full articles or review articles in biological sciences, material sciences or education to either journal editor.

Catalina Pislariu
cpislariu@twu.edu

Nabarun Ghosh
nghosh@wtamu.edu

Corporate Members and Regional Sales Managers



Advanced Microscopy Techniques
<http://www.amtimaging.com>
Tom Levesque
242 West Cummings Park
Woburn, MA 01801
Tel: 972-966-0865
tlevsque@amtimaging.com



DRVision Technologies (AIVIA)
www.aivia-software.com
Trevor Lancon
15921 NE 8th St., Suite 200
Bellevue, WA 98008
Tel: 855-423-5577
trevorl@drvtechnologies.com



AMETEK
<http://www.ametek.com>
Sue Arnell
85 Mckee Dr.
Mahwah, NJ 07430-2105
Tel: 201-529-4880
sue.arnell@ametek.com



AVR Optics
www.avr-optics.com
Lane Manning
187 N Water Street
Rochester, NY 14604
Tel: 585-445-7588
lane.manning@avr-optics.com



BioTek Instruments, Inc. (Now Agilent)
<http://www.biotek.com>
Vanessa Meyer
5301 Stevens Creek Blvd.
Santa Clara, CA 95051
Tel: 800-227-9770
meyerv@biotek.com



Bruker AXS, Inc.
www.bruker.com
John Mastovich
3194 Beverly Court
Murrysville, PA 15668
Tel: 908-419-8225
Austin, TX 78747
john.mastovich@bruker.com



CARL ZEISS SMT
<http://www.zeiss.com/nts>
Laura Grafflin
One corporation Way
Peabody, MA 01960
Tel: 978-826-1500
Fax: 978-532-5696 Fax
laura.grafflin@zeiss.com



Discover Echo Inc.
<https://discover-echo.com/>
Brian Templin
9530 Padgett St., Suite 101
San Diego, CA 92126
btemplin@discover-echo.com



Electron Microscopy Science/Diatome
<http://www.emsdiasum.com/microscopy/>
Stacie Kirsch
1560 Industry Road, P.O. BOX 550
Hatfield, PA 19440
Tel: 800-523-5874
Fax: 215-412-8450
Stacie@ems-secure.com



Fischione Instruments, Inc.
<http://www.fischione.com>
Nicole Dengler
9003 Corporate Circle
Export, PA 15632
Tel: 724-325-5444
nm_dengler@fischione.com



Hitachi High Technologies America
<http://www.hitachi-hta.com>
Rod Baird
1375 North 28th Ave.
PO Box 612208
Irving TX 75261
Tel: 214-537-2158
Fax: 972-615-9300
rod.baird@hitachi-hta.com



IXRF Systems
<http://www.ixrfsystems.com>
Mandi Hellested
10421 Old Manchaca Rd., Suite 620
Austin, TX 78748
Tel: 512-386-6100
Fax: 512-386-6105
mandih@ixrfsystems.com



Solutions for Innovation
JEOL USA, Inc.
<http://www.jeolusa.com>
Zane Marek
13810 Paisano Circle
Austin, TX 78737
Tel: 978-495-2176
marek@jeol.com



Leica Microsystems, Inc.
<http://www.leica-microsystems.com>
Kraig Valadez
7125 Northland Terrace N., Suite 100
Brooklyn Park, MN 55428
Tel: 314-374-9361
Kraig.Valadez@leica-microsystems.com



M.E. Taylor Engineering, Inc.
<http://www.semsupplies.com>
SEMico Division
15817 Crabbs Branch Way
Rockville, MD 20855
Tel: 301-975-9798
sales@semicro.org



NCI Micro
<http://www.microstartech.com>
 Mike Hehr
 Brooklyn Park, MN 77340
 Tel: 888-559-3312
Mikeh@ncimicro.com



Molecular Devices, LLC.
<https://www.moleculardevices.com/>
 Robert Moody
 3860 North First Street
 San Jose, CA 95134
 Tel: 800-635-5577
robert.moody@moldev.com



Nikon Instruments Inc.
<http://www.nikoninstruments.com>
 Clay Williams
 1300 Walt Whitman Road
 Melville, NY 11747-3064
 Tel: 972-693-7779
sidney.williams@nikon.com



Olympus Corp.
www.olympus-lifescience.com
 Brian Cook
 48 Woerd Ave.
 Waltham, MA 02453
 Tel: 512-230-5624
Brian.Cook@Olympus-ossa.com



Oxford Instruments America, Inc.
www.oxford-instruments.com
 Dave Richards
 300 Baker Avenue, Suite 150
 Concord, MA 01742
 Tel: 978-369-9933 x 201
david.richards@oxinst.com



Park Systems Inc.
<https://www.parksystems.com>
 Doru Florescu
 3040 Olcott St.
 Santa Clara, CA 95054
 Tel: 408-985-1110
 Fax: 408-986-1199
doru@parksystems.com



Protochips
www.protochips.com
 Steve Shannon
 3800 Gateway Centre Blvd., Suite 306
 Morrisville, NC 27560
 Tel: 919-377-0898
Steve.Shanon@protochips.com



Rigaku
www.rigaku.com
 Michelle Goodwin
 9009 New Trails Dr.
 The Woodlands, TX 77381
 Tel: 281-362-2300 ext. 122
Michelle.Goodwin@rigaku.com



Boeckeler Instruments, Inc.
<http://www.boeckeler.com>
 Todd Perez
 4650 S. Butterfield Drive
 Tucson, AZ 85714
 Tel: 520-745-0001
 Fax: 520-745-0004
todd.perez@boeckeler.com



Ted Pella, Inc.
<http://www.tedpella.com>
 James Long
 PO Box 462477
 Redding, CA 96049-2477
 Tel: 530-243-2200 or 800-237-3526
James_Long@tedpella.com



TESCAN USA, Inc
<http://www.tescan-usa.com>
 Mike Craig
 765 Commonwealth Drive, Suite 101
 Warrendale, PA 15086
 Tel: 512-417-8990
mike.craig@tescan-usa.com



Texas State University
 Shared Research Operations
<https://sro.txstate.edu/>
 Casey Smith
 601 University Drive
 San Marcos, TX 78666
 Tel: 512-245-6635
cs53360@txstate.edu

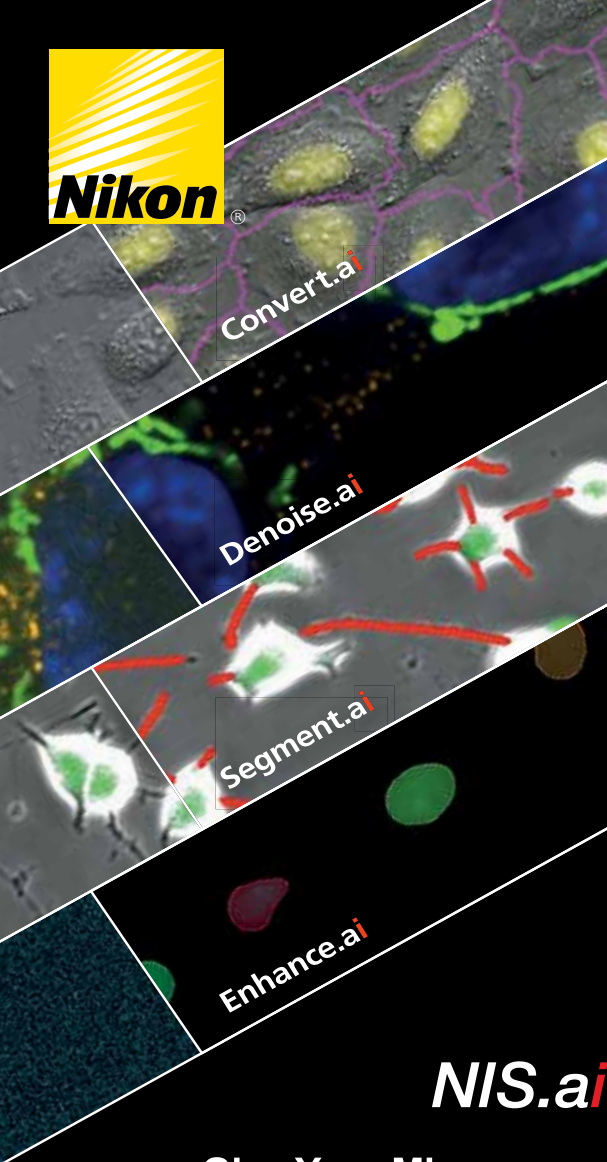


Thermo Fisher Scientific
<https://www.thermofisher.com>
<http://www.fe.com>
 Ciceron Yanez
ciceron.yanez@thermofisher.com
 Dan Gostovic
dan.gostovic@thermofisher.com
 Bill Sgammato
bill.sgammato@thermofisher.com



Tousimis
<http://www.tousimis.com>
 Hyun Park
 2211 Lewis Avenue
 Rockville, MD 20851
 Tel: 301-881-2450
 Fax: 301-881-5374
hjpark@tousimis.com





NIS.ai

**Give Your Microscope
the Power of
Artificial Intelligence**



Nikon is here for you, deep in the heart of Texas...

- | | |
|---|--------------|
| Michael Johnson, <i>Regional Manager</i> | 214-738-0120 |
| Clay Williams, <i>Bioscience Sales Specialist</i> | 972-693-7779 |
| Kara Harmatys, <i>Bioscience Sales Specialist</i> | 713-301-9932 |
| Renata Tully, <i>Bioscience Sales Specialist</i> | 469-381-4669 |
| Mark Nilges, <i>Bioscience Sales Specialist</i> | 504-343-2334 |
| Jon Ekman, <i>Bioscience Sales Specialist</i> | 407-595-6542 |
| Joshua Deal, <i>Bioscience Sales Specialist</i> | 405-617-6014 |
| Kalika Landua, <i>Advanced Imaging Specialist</i> | 713-542-0410 |
| Anil Shukla, <i>Advanced Imaging Specialist</i> | 512-839-5886 |
| Kevin Lam, <i>Advanced Imaging Specialist</i> | 214-551-3113 |
| Jacob Burnett, <i>Advanced Biosystems Specialist</i> | 713-205-6366 |
| Matthew Mitschelen, <i>Senior Biosystems Applications Manager</i> | 972-400-0258 |



ATUMtome

The Standard in 3D Reconstruction Sample Preparation

ATUMtome Automated Tape Collecting Ultramicrotome

Collect hundreds to thousands of sections on a continuous tape

Non-destructive to sample

Store sections for years into the future for processing, post-staining, immunogold labeling, correlative imaging - at any work pace desired

Patented Power Drive® for biological samples and extremely hard materials



POWERFUL MODULAR PRECISE

RMC
Boeckeler

www.boeckeler.com

Discover our range of microscopy sample preparation systems and workflow instruments